Available online at www.sciencedirect.com

ScienceDirect

Geochimica et Cosmochimica Acta 209 (2017) 161–183

Geochimica et Cosmochimica Acta

www.elsevier.com/locate/gca

Low temperature hydrogen production during experimental hydration of partially-serpentinized dunite

Hannah M. Miller [a,*], Lisa E. Mayhew [a], Eric T. Ellison [a], Peter Kelemen [b], Mike Kubo [c], Alexis S. Templeton [a,1]

[a] Department of Geological Sciences, UCB 399, University of Colorado, Boulder, CO 80309, USA
[b] Lamont-Doherty Earth Observatory of Columbia University, 61 Route 9W, Palisades, NY 10964, USA
[c] Carl Sagan Center for Life in the Universe, SETI Institute, Mountain View, CA 94043, USA

Received 7 September 2016; accepted in revised form 14 April 2017; available online 24 April 2017

Abstract

Dissolved hydrogen is common in mafic and ultramafic aquifers; however, the water/rock reactions that give rise to hydrogen production at near-surface temperatures are enigmatic. Similarly, mineral hydration experiments have not yet unequivocally demonstrated whether H_2 can be produced at low-temperatures at significant rates from reaction of aqueous fluids with basalts and peridotites for prolonged amounts of time. We conducted laboratory-based water/rock reactions between partially serpentinized Oman dunite and a simulated Oman rainwater (RW) media, as well as a simulated seawater (SW) media, to quantify H_2 generation rates at 100 °C. Throughout more than 9 months of water/rock reaction, extensive hydrogen production and consumption were observed in RW and SW media. In the first 24 h of reaction in anoxic fluids containing only dissolved N_2 and CO_2, the room-temperature pH in both RW and SW media increased from 6.5 to ~9, and the average pH then remained relatively constant at pH 8.5 (±0.5 pH) for the duration of the experiments. We also measured some of the highest hydrogen concentrations observed in experimental low-temperature serpentinization reactions. The maximum measured H_2 concentrations in SW media were 470 nmol H_2 per g mineral after ~3 months, while RW media H_2 concentrations reached 280 nmol/g H_2 after ~3 months. After reaching micromolar dissolved $H_{2(aq)}$, the H_2 concentrations notably declined, and CO_2 was almost fully consumed. We measured the formation of formate (up to 98 μM) and acetate (up to 91 μM) associated with a drawdown of H_2 and CO_2 in the experiments. No CH_4 or carbonate formation was observed. To identify reactions giving rise to low-temperature hydrogen production, the mineralogy and oxidation state of the Fe-bearing species in the dunite were extensively characterized before and after reaction using Raman spectroscopy, Quantitative Evaluation of Minerals by SCANing electron microscopy (QEMSCAN), powder X-ray diffraction (XRD), magnetic susceptibility, scanning electron microscopy (SEM), and Fe K-edge X-ray absorption near edge structure (XANES) spectroscopic techniques. The mineralogy of the solid starting material was dominated by olivine and serpentine with minor brucite, pyroxene and spinel. After reaction, additional serpentine and magnetite could be detected as reaction products, and pre-existing brucite was consumed. No changes were observed in the abundance or grain sizes of olivine or pyroxene. Thus, we propose that the destabilization of Fe(II)-bearing brucite and the subsequent oxidation of the aqueous Fe(II) to form magnetite and Fe(III)-rich serpentine give rise to H_2 production at 100 °C. This work demonstrates that dissolved hydrogen and low molecular weight organic acids can be produced by the reaction of labile Fe

---

* Corresponding author.
E-mail addresses: hannah.miller-1@colorado.edu (H.M. Miller), alexis.templeton@colorado.edu (A.S. Templeton).
[1] Co-corresponding author.

http://dx.doi.org/10.1016/j.gca.2017.04.022

(II)-bearing minerals generated during a prior stage of water/rock reactions. In particular, progressive alteration of partially-serpentinized peridotites containing brucite may generate sufficient electron donors to fuel in-situ subsurface microbial activity.

Keywords: Serpentinization; Hydrogen; Low-temperature; Brucite

1. INTRODUCTION

Serpentinization, the hydration and oxidation reaction of ultramafic rocks and minerals, can produce hydrogen at low temperatures which can support H_2-fueled microbial life (Sleep et al., 2004; Nealson et al., 2005; Mayhew et al., 2013). Low-temperature reactions can be classified as those occurring $\leq$122 °C (Takai et al., 2008), which is the highest temperature of observed microbial growth. Serpentinization reactions are predicted to produce less hydrogen at temperatures relevant for microbial life, but still enough to sustain subsurface microbial ecosystems, which can utilize H_2 concentrations as low as 13 nM (Kral et al., 1998; Nealson et al., 2005). H_2-fueled metabolisms are diverse and include anaerobic methanotrophy, fermentation, sulfate reduction and hydrogen oxidation tied to iron reduction (Schrenk et al., 2013). H_2 produced by serpentinization reactions may have fueled the first life on Earth at low-temperature off-axis hydrothermal fields (Russell et al., 2010, 2013; Shibuya et al., 2016). Additionally, serpentinization reactions have likely occurred on Enceladus and Mars, which may provide a favorable environment for H_2-utilizing microbial life (Ehlmann et al., 2010; Glein et al., 2015; Sekine et al., 2015).

However, the mechanisms and reaction pathways giving rise to hydrogen production at low temperatures are unclear (Stevens and McKinley, 1995; Anderson et al., 1998; Neubeck et al., 2011, 2014; Mayhew et al., 2013; Okland et al., 2014; Telling et al., 2015), whereas high temperature (>200 °C) hydrogen production is well-characterized through both experimental and modeling efforts (Fyfe, 1974; McCollom and Seewald, 2001; McCollom and Bach, 2009; Klein et al., 2009, 2013, 2015; Evans et al., 2009; Malvoisin et al., 2012a,b; Frost et al., 2013; McCollom et al., 2016). Thus, further work on low-temperature serpentinization and associated hydrogen production is necessary to better constrain reaction pathways and mechanisms (Mayhew et al., 2013; Bach, 2016; McCollom and Donaldson, 2016).

Although extensive thermodynamic modeling of hydrogen production has been conducted at high temperatures, these results cannot be easily extrapolated to lower temperatures. Several thermodynamic models have been used to infer that water/rock reactions at low temperatures will generate much less hydrogen than at temperatures from 200 to 350 °C (McCollom and Bach, 2009; Klein et al., 2009, 2013). Hydrogen production at temperatures <120 °C is predicted to strongly decrease because Fe(II) released from olivine will be sequestered into secondary brucite, resulting in less Fe oxidation. Magnetite formation is also thermodynamically inhibited at low temperatures (McCollom and Bach, 2009; Klein et al., 2013). Instead, the formation of Fe(III)-rich serpentine may be the central reaction accommodating low-temperature hydrogen generation. Thermodynamic models also assume systems reach a state of equilibrium, and this may not occur during fluid flow through peridotite aquifers (Paukert et al., 2012). Also, the kinetics and mechanisms of the key mineral dissolution, precipitation and Fe(II)-oxidation reactions are poorly constrained, along with the thermodynamic data for Fe(III) secondary phases that form at low temperatures.

Although recent kinetic-thermodynamic modeling of reactions between peridotite and water at 25 °C (Bach, 2016) addresses some of these issues, it is clear that these models need to be experimentally verified. Further mechanistic studies are needed to reveal the rates and reactions involved in H_2 production during low temperature peridotite alteration. New models by Bach (2016) better capture the complexity of these low-temperature reactions by allowing the precipitation of several possible Fe(III) reaction products to accommodate H_2 production. Notably, these new models predict that more H_2 could be produced at low temperatures than has been observed experimentally (e.g. in Mayhew et al. (2013) and Neubeck et al. (2011), etc.). Experiments coupled with new models may help to explain how continental ophiolite systems contain high concentrations of dissolved hydrogen at near surface temperatures (Neal and Stanger, 1983; Abrajano et al., 1990; Etiope et al., 2011; Morrill et al., 2013; Szponar et al., 2013; Suda et al., 2014; Miller et al., 2016).

Several experimental studies of water/rock reactions have investigated the rates and extent of low-temperature H_2 generation (Stevens and McKinley, 1995; Anderson et al., 1998; Neubeck et al., 2011, 2014; Mayhew et al., 2013; Okland et al., 2014; Telling et al., 2015), yet they have encountered numerous challenges and have produced inconsistent results (Table 1). It is difficult to reproduce results as a variety of conditions can affect the amount of hydrogen production (Stevens and McKinley, 1995, 2000; Anderson et al., 1998). These factors include water/rock ratio, fluid chemistry, pH, temperature, silica activity, surface passivation, mineral surface area, composition of the reaction vessel, and Fe(II/III) partitioning into secondary mineral phases (Béarat et al., 2006; Frost and Beard, 2007; McCollom and Bach, 2009; Klein et al., 2009; Mayhew et al., 2013; Andreani et al., 2013). Challenges arise from the fact that reactions are oftentimes conducted in silica serum vials with butyl stoppers that generate small amounts of hydrogen (Anderson et al., 1998; Mayhew et al., 2013; McCollom and Donaldson, 2016). Additionally, incomplete serpentinization of starting material and slow reaction rates make it difficult to judge the true

Table 1
Comparison of maximum experimental hydrogen generation measured at temperature <100 °C.

Study	Temperature (°C)	Max. H_2 generation (nmol/g mineral)	Rock/mineral reacting	pH	Water:rock ratio	Mineral surface area (m^2/g) or mineral diameter (mm)
Stevens and McKinley (1995)	22	~80	Umtanum Ridge Basalt	6	1–1	<0.25 mm
Anderson et al. (1998)	22	500	Snake River Plain basalt	6	1–1	0.53–0.125 mm
Stevens and McKinley (2000)	60	~60	Reference Umtanum Colonnade basalt	5	1–1	1 m^2/g
Neubeck et al. (2011)	30	0.24	Olivine (Forsterite 91)	9.07	2.3–1	0.125–1.0 mm
Mayhew et al. (2013)	100	300	San Carlos peridotite	~7	7–1	0.34 m^2/g
Okland et al. (2014)	25	~110	Highly altered Leka ophiolite dunite	9.56	2–1	7.1 m^2/g
Telling et al. (2015)	0	~10	Elsworth quartzite	NA	1–1	~1–4 m^2/g
Telling et al. (2015)	35	~60	Engabreen schist	NA	1–1	~6–12 m^2/g
McCollom and Donaldson (2016)	90	39.6	Harzburgite	6.8	4–1	0.59 m^2/g
This study	100	500	Partially serpentinized Oman dunite	9	7–1	0.47–0.60 m^2/g

hydrogen-generating potential of the minerals and rocks reacted (Neubeck et al., 2011, 2015; Okland et al., 2012, 2014; Mayhew et al., 2013). The low extent of reaction also makes it difficult to quantify mass changes and determine the operative Fe-oxidation pathways (Mayhew et al., 2013). Thus, experimental studies of low-temperature serpentinization which encompass the entire, complex reactions involved in water/rock reactions with environmentally relevant, partially altered rocks are needed.

1.1. This study

This study investigates hydrogen production from laboratory water/rock reactions between partially serpentinized dunite from Oman and anoxic fluids at low temperatures (100 °C). The dunite is ~50% serpentinized, which constitutes some of the least-altered rocks from the Samail ophiolite. This is the world's largest and best exposed ophiolite, which contains large reserves of peridotite and an extensive aquifer system where deep subsurface hyperalkaline fluids contain millimolar amounts of dissolved hydrogen at temperatures <50 °C (Barnes et al., 1978; Neal and Stanger, 1984; Kelemen et al., 2011; Streit et al., 2012; Miller et al., 2016).

We simulated serpentinization reactions between anoxic fluids and Oman dunite, and observed extensive H_2 production and consumption over >9 months of water rock reaction at 100 °C. Partially serpentinized dunite OM95-35 was chosen for this work as representative of a typical dunite obtained from a surface outcrop in Oman; there are numerous olivine-rich dunite lenses in the mantle section of the Samail ophiolite (Kelemen et al., 1997; Hanghøj et al., 2010). We probed the changes in mineralogy and aqueous geochemistry of the minerals and fluids to infer the reactions associated with H_2 generation. The whole rock mineralogy of the dunite, as well as the mineralogy of the rock powders after water/rock reaction, have been characterized with powder XRD, XANES spectroscopy, Raman spectroscopy, QEMSCAN, magnetic susceptibility techniques, and thermogravimetric analysis (TGA). By coupling this data with changes in dissolved ions, gases and organic acid concentrations, we identify the key reactions that give rise to H_2 production in our experimental system.

2. METHODS

2.1. Experimental set-up

We prepared 70 mL silica serum vials of medium-only blanks and water/rock reactions (Fig. 1). The experiments were conducted with two different solution compositions: an artificial seawater medium (SW) and a simulated Oman rainwater medium (RW, Table 2). The artificial SW medium contained 27.5 g/L NaCl, 1.4 g/L $CaCl_2$, 0.72 g/L KCl, 0.2 g/L $NaHCO_3$, 1.0 g/L NH_4Cl, 0.05 g/L K_2HPO_4, and 5.38 g/L $MgCl_2$ and is identical to the solution composition in Mayhew et al. (2013). The simulated Oman RW medium contained 9.89 mg/L NaCl, 11.10 mg/L $CaCl_2$, 5.06 KNO_3, 7.41 $Ca(OH)_2$, 30.83 $CaSO_4 \cdot H_2O$, 12.32 $Mg(SO_4)_2 \cdot 7H_2O$, and 10.17 mg/L $MgCl_2$ (from Paukert et al. (2012)). Five grams of partially serpentinized Oman dunite were mixed with 35 mL of the specified medium to achieve a water/rock ratio of 7 (Mayhew et al., 2013). The vials were purged with 80% N_2:20% CO_2 to achieve anoxic conditions and placed in a 100 °C oven to react. This temperature was chosen to ensure reaction along reasonable time-scales in temperature ranges relevant to microbial life. Additionally, two vials containing Oman dunite, filled with SW and RW media, respectively, were purged with 100% N_2 gas to investigate low-weight molecular acid formation without added headspace CO_2 (Fig. 1).

Prior to use, the silica serum vials were heated to 550 °C for 3 h to remove any combustible carbon species. The vials were capped with an airtight butyl rubber stopper boiled 3 times in 0.1 N NaOH media following the protocol of Oremland et al. (1987) to reduce contamination by volatile organic compounds in the butyl stoppers. Vials, rubber stoppers, and the media were autoclaved before the experiment began.

The Oman dunite was cut with a diamond-blade saw; the outer weathered portions of the rock were removed and only the unweathered interior was used in experiments. The rock was tumbled with silicon carbide in a rock tumbler with de-ionized water, rinsed, and then tumbled again with fresh silicon carbide to remove any residual steel fragments from sampling/sawing, which could produce hydrogen by the reaction of Fe(0) with water. The cleaned material was crushed with a ceramic mortar and pestle and wet-sieved with deionized water to a size fraction of 53–212 μm. The surface area (SA) of the unreacted and reacted minerals was determined with the Brunauer–Emmett–Teller (BET) method using a Micromeritics Gemini V machine with N_2 gas.

H_2 in SW experiments was measured for 203 days, but the vials continued to react in the 100 °C oven after regular H_2 analysis ended, which allowed us to sample pH, fluid, and mineral grains at later time points (Table 3). H_2 in RW experiments was measured for 97 days, and these vials also continued to react in the 100 °C oven after this time period. Small amounts of fluid (<0.5 mL) were sampled from SW vials periodically to measure pH, whereas 2 mL of fluid was sampled periodically from RW vials to fully analyze aqueous geochemistry and pH. When 2 mL of fluid was removed from RW vials, it was replaced with equal volumes of fresh N_2-purged RW medium to preserve the water/rock ratio of 7.

Sampling for H_2 gas, water chemistry, and reacted mineral products was not uniform across experimental sets. Thus, the information is summarized in Table 3 to clearly show when various samples were extracted. H_2 gas monitoring stopped after 203 or 97 days because the H_2 concentrations were no longer increasing or noticeably changing. The experiments were maintained at 100 °C to allow for sampling of the reacted rock at later times. As a result, most of the reacted samples were obtained after hydrogen monitoring was complete. Mineral grains were not all sampled at the same time because additional analyses were performed as needed to fully characterize the mineralogical and geochemical changes. Grains removed from the water/rock reactions were extracted with a 23 gauge needle and rinsed 3 times with de-ionized (DI) water before analysis. Some of this material was mounted in epoxy for microscale analysis, while some remained in dried loose powder form. We are aware there was likely size discrimination during this removal process, but it was the best method available to us to allow continued reaction of the additional rock.

H_2 in the experiments was measured on an SRI 310C gas chromatograph with an Alltech Molecular Sieve (5A 80/100) 6000-8500 ID column and thermal conductivity detector using N_2 as the carrier gas. 0.5 mL of headspace gas was sampled for this analysis, thus, vials developed a

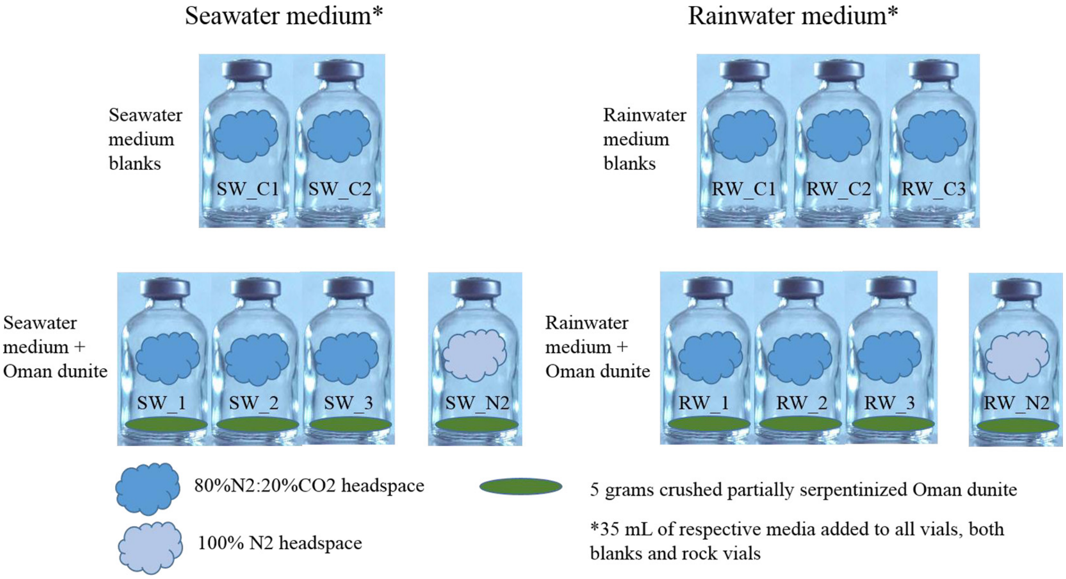

Fig. 1. Experimental matrix for water/rock reactions and blanks. 13 Vials total were prepared and monitored over the lifespan of the experiments.

Table 2
Composition of initial SW and RW media prior to water/rock reaction, as calculated from media formulation. This fluid was equilibrated with a 80% N_2:20% CO_2 headspace. Concentration of HCO_3^- in media includes solid bicarbonate included in media and HCO_3^- generated from the dissolution and speciation of headspace CO_2.

	Starting composition (mM)	
	SW media	RW media
pH	7	6.5
Na^+	470.57	0.20
Ca^{2+}	12.61	0.50
K^+	10.23	0.05
Mg^{2+}	26.46	0.15
Cl^-	577.08	0.50
NO_3^-	0.00	0.05
SO_4^{2-}	0.00	0.30
HCO_3^-	2.41	0.02
NH_4^+	18.69	0.00
HPO_4^{2-}	0.29	0.00

partial vacuum over time because the headspace samples were not replaced with any additional gas. The H_2 standard concentrations were calibrated each time the machine was used which led to some of the variability observed in the H_2 concentrations between measurements. However, the standard values varied by less than 5%, so overall trends are valid. A separate GC was used to measure CH_4 and CO_2. Methane was measured using a flame ionization detector and CO_2 was measured using a thermal conductivity detector on an SRI 8610C gas chromatograph with a PORAPAK Q 60_0:085” I.D. column using He as the carrier gas. H_2 and CH_4 detection limit is ~10 nmol and the overall measurements have a variability of 5%.

To test the rate of H_2 diffusion out of the butyl stoppers, we incubated three empty silica serum vials purged with 10%H_2:90%N_2 at 100 °C for 425 days and periodically measured H_2 headspace concentrations (Supplementary Fig. 1). This test shows an average of 20 nmol of headspace H_2 leaks from the vials per day. However, the amount of hydrogen in the headspace of these test measurements is much larger (158 μmol) than the hydrogen in our experiments (2.4 μmol). Thus, we scaled the rate of hydrogen diffusion down to match the experimental hydrogen levels (Supplementary Fig. 1), which then shows a prediction that approximately 1 nmol of H_2 would be lost per day. A similar control experiment was conducted to document the release of Si from serum vials over time. Three serum vials were filled with 35 mL of artificial SW medium and incubated for 51 days, with periodic sampling for aqueous Si (Supplementary Table 1). The results show an increase of ~2.7 μM aqueous Si daily, which we acknowledge when discussing some of the mineral dissolution and precipitation reactions.

2.2. Aqueous geochemistry of the water/rock reactions

Major and minor elemental data was only collected for RW vials during water/rock reaction, and all fluid samples were replaced by an equal volume of the anaerobic media. Trace elements (Ni, Cr) were analyzed on acidified and filtered fluid from the water/rock reactions using Inductively Coupled Plasma-Mass Spectrometry (ICP-MS) on a Perkin Elmer SCIEX Elan DRC-e. Major cations ($SiO_{2(aq)}$, Mn^{2+}, Fe^{2+}, Mg^{2+}) were analyzed using Inductively Coupled Optical Emission Spectrometry (ICP-OES) on an ARL 3410+ with a Meinhard nebulizer. The detection limits were 0.345 μM for Si, 0.026 μM for Mn, and 0.111 μM for Mg. These analyses were conducted at the Laboratory for Environmental and Geological Studies (LEGS) at the University of Colorado at Boulder. Water samples (5 mL) for both SW and RW vials were collected in acid-washed, autoclaved, and ashed organic free vials and sent to NASA Ames Research Center to measure low weight molecular organic acids on a Shimadzu Prominence LC20AT high-performance liquid chromatograph (HPLC) equipped with a SPD-M20A photodiode array detector and a flow rate of 1 mL per min. pH was measured with a Thermo Scientific Orion PerpHecT ROSS Combination pH Micro Electrode calibrated with reference standards of pH 4, 7, and 10. The pH was measured at 25 °C, whereas the water/rock reactions were incubated at 100 °C. We are unable to report the in situ pH at 100 °C because of incomplete aqueous geochemical and gas headspace data for each corresponding pH measurement. However, we did explore pH re-speciation based on temperature using the React module in Geochemist Workbench v8 with the standard thermodynamic dataset. The resulting pH varied from 6 to 7.8 depending on whether we suppressed the formation of carbonate minerals. Thus the in-situ pH values cannot be determined with the available data, but the in-situ pH will be lower than the pH measured at 25 °C.

2.3. Characterizing the mineralogy of the partially serpentinized dunite pre- and post-reaction

The surface area (SA) of the unreacted and reacted crushed Oman dunite was determined with the Brunauer–Emmett–Teller (BET) method using a Micromeritics Gemini V machine with N_2 gas at the University of Colorado at Boulder. Quantitative powder XRD analyses were conducted on the unreacted dunite and a serpentine standard to determine initial modal mineralogy at the Campbell laboratory at the Boulder United States Geological Survey. Samples were prepared for XRD using a modified method based on Eberl (2003). One gram of homogenized sample was mixed with 20% corundum and ground in a McCrone micronizing mill with 4 mL ethanol for 5 min, generating particle sizes on the order of 10–30 μm. The resulting sample was dried at 50 °C in an oven overnight and then combined with 500 mL of DuPont™ Vertrel® and mixed for 10 min with 3 delrin balls in a Spex SamplePrep 8000D Mixer/mill to preserve random crystal orientations during the packing step. The powder was passed through a 250 μm sieve to break up larger aggregates, and loaded into a side-mounted XRD sample holder (Eberl, 2003). Samples were analyzed using a Siemens D500 X-ray diffractometer from 5° to 65° 2Θ using Cu Kα X-ray radiation, with a step size of 0.02° and a dwell time of 2 s per step. The sample rotates during the scanning process at 30 rpm, thus

Table 3
Sampling timeline for all analyses. The SW & RW days columns indicate when the sample was collected with respect to days from the start of the water/rock reactions. Samples were extracted at different times from SW and RW vials in an attempt to thoroughly characterize all geochemical changes during reaction.

Sample	Analysis performed	SW vials (days)	RW vials (days)	Data figure
Gas and aqueous samples				
H_2 gas sampling (0.5 mL headspace gas)	Gas chromatography for H_2	0–203^{+}	0–97^{+}	Fig. 5 and Tables 6 and 7
CO_2 gas sampling (single time point, 0.5 mL headspace gas)	Gas chromatography for CO_2	304	171	Supplemental Table 5
Fluid for aqueous geochemistry (2 mL)	ICP-OES ($SiO_{2(aq)}$, Mn^{2+}, Fe^{2+}, Mg^{2+}, Ca^{2+}) ICP-MS (Ni, Cr) IC (SO_4^{2-})	Only 287	0–155	Fig. 6
Fluid for pH sampling (<0.5 mL)	pH measurement	0–287	0–366	Supplemental Fig. 3
Fluid for organic acid sampling* (5 mL)	HPLC measurement for low weight molecular organic acids	525	392	Table 8
Mineral samples				
Unreacted rock samples				
Thin section of unreacted Oman dunite	QEMSCAN, Raman spectroscopy, µXANES mapping, electron microprobe	0	0	Figs. 3, 4, Table 5 and Supplementary Figs. 2 and 5
Unreacted mineral grain mount	XANES, electron microprobe	0	0	Supplementary Fig. 5 and Table 5
Unreacted mineral grains	Quantitative powder XRD, bulk XANES, BET, TGA, SQUID magnetometer, TOC	0	0	Tables 4 and 9, Figs. 2 and 10
Reacted rock samples				
Mineral sample extracted from vials	Raman spectroscopy, BET, SEM, XRD, µXANES, electron microprobe, length of olivine grains analyzed	111 and 330**	NA	Fig. 9 and Supplementary Table 3
Mineral sample extracted from vials	Raman spectroscopy, BET, TGA, µXANES (bulk and microscale), length of olivine grains analyzed	NA	275	Figs. 9 and 10 and Supplementary Table 3
White mineral precipitate extracted	Powder XRD (only SW sample), Micro-Raman spectroscopy, SEM	111	90	Figs. 7 and 8 and Supplementary Figs. 2 and 4
Vial opened and all 5 g of mineral extracted	Quantitative powder XRD, Total organic carbon analysis, mass spectrometer to quantify CO_2, SQUID magnetometer, bulk XANES, Raman spectroscopy	>730	>365	Fig. 2 and Supplementary Fig. 5, Tables 2 and 4

$^{+}$ Continued reacting the vials in the oven, but did not monitor regularly after this time period.
* 100% N_2 purged vials were both sampled after 308 days of reaction with same protocol.
** the second SW sample extracted at 330 days was only analyzed with µXANES and electron microprobe techniques.

ensuring a representative scan of the sample's surface. Fitting was determined with USGS software, RockJock, a program that quantifies the mineralogy of powdered samples by comparing the integrated XRD intensities of minerals in mixtures to intensities of an internal corundum standard (Eberl, 2003).

TGA measurements were taken in a NETZSCH STA 449 F1 Jupiter at the University of Colorado at Boulder. Between 60 and 110 mg of sample in an alumina crucible and a blank alumina crucible were heated in Argon up to 1000 °C at a ramp rate of 10 °C per min. The crucibles were held at 1000 °C for one hour, at which point data collection stopped and the furnace cooled. The derivatives of the data were determined using NETZSCH Proteus.

QEMSCAN, at Colorado School of Mines, was also used to identify the mineralogy and textural relationships of a thin section of unreacted dunite. QEMSCAN integrates scanning electron microscope (SEM) analysis with energy dispersive X-ray spectrometry (EDS) and calibrated backscatter electron (BSE) intensity levels to generate a mineralogy map of the thin section (Hoal et al., 2009). The instrument operated at 25 kV accelerating voltage, 5 nA sample current, 1 µm beam size with a step size of 5 µm.

Micro-Raman spectra of unreacted and reacted grains, and a hyperspectral map of the unreacted dunite thin section were collected using a Horiba LabRAM HR Evolution Raman spectrometer at the Department of Geological Sciences at the University of Colorado at Boulder equipped with a 532 nm frequency-doubled Nd:YAG laser coupled to an Olympus BXFM optical microscope. The laser beam was focused through a 50× (0.75NA) objective lens, yielding a spatial resolution of ~2 µm. A 600 lines/mm grating and adjustable confocal pinhole (100–200 µm) were used to give a spectral resolution full width at half maximum (FWHM) of 4.5–8.4 cm^{-1}. Spectra were collected using a

Si-based CCD detector (1024 × 256 pixels). The spectrometer was calibrated daily using the 520 cm^{-1} Raman peak of Si prior to analysis. Spectral data were corrected for instrumental artifacts and baseline-subtracted using a polynomial fitting algorithm in LabSpec 6 (Horiba Scientific). A hyperspectral map of a representative area in the thin section was generated using Multivariate Curve Resolution-Alternating Least Squares (MCR-ALS). Non-negativity constraints on scores and loadings were determined for the main spectral components present, then spot Raman spectra were collected to verify the components, and the hyperspectral data set was fit with the end member spectra to generate component maps.

Synchrotron-based hard X-ray measurements of Fe K-edge micro-X-ray absorption near edge spectra (μXANES) were conducted at Beamline 2–3 at the Stanford Synchrotron Radiation Lightsource (SSRL). The incident energy was selected with a Si (111) double crystal monochromator with the SPEAR accelerator ring containing ~350–500 mA at 3.0 GeV. The beam was focused to approximately 2 by 2 μm using Kirkpatrick Baez mirrors. Data were collected at the Fe K-edge using a Fe^0 foil calibration of 7112 eV with a single-element Vortex detector capable of counting several million counts per second. Fe K-edge XANES spectra were collected from 6882 to 7505 eV with a high resolution (step size of 0.1 eV) through the pre-edge (7108–7118 eV) region and a dwell time of 3 s. The acquisition time is 16 min, thus some photo-oxidation may have occurred, which may result in slightly over-estimated Fe^{3+}/Fe_{total} ratios (Debret et al., 2014). Crystal orientation leads to varying measurements of pre-edge centroids, which can also shift Fe^{3+}/Fe total ratios by 0.1 in antigorite (Muñoz et al., 2013). XANES were background subtracted and normalized with Sam's Interface for XAS Package (SIXPACK). Analysis of the pre-edge to determine the ratio of Fe^{2+}/Fe_T employed protocols from Andreani et al. (2013) and Wilke et al. (2001). Measurement, analysis, and comparison of the pre-edge of standards with known Fe(II)/(III) ratios and Fe coordination states (staurolite, andradite, sanidine and siderite provided and previously characterized by Dr. Manuel Muñoz) to unknown samples allows us to constrain the Fe(II)/(III) ratio in primary and alteration phases in order to assess the extent of Fe oxidation and the distribution of Fe(II) vs. Fe(III) between different mineral phases.

Beamline 4–1 at SSRL was used to collect bulk Fe K-edge spectra for powdered samples. A Si (220) $\phi = 0$ monochromator was used and X-ray absorption spectra (XAS) were collected on a Lytle detector. A Fe^0 foil standard was used and calibrated to 7112 eV. Duplicate spectra were collected and averaged for XANES scanning from a range of 6882–7082 eV with a step size of 10 eV, then from 7092 to 7520 with a 0.35 eV step size. Calibration of the Fe pre-edge was not conducted.

The Quantum Design MPMS Superconducting Quantum Interference Device (SQUID) magnetometer with magnetic moment resolution of 10^{-8} emu at the Department of Physics and Astronomy at Michigan State University was used to analyze two bulk rock powder samples to determine magnetic hysteresis parameters over the range of ±5 T at 300 K.

Quantitative chemical analysis of serpentine was performed using the electron microprobe laboratory at the University of Colorado at Boulder on the JEOL JXA-8600 equipped with 4 wavelength-dispersive spectrometers, and a PGT energy-dispersive spectrometer. Spot analyses of polished thin sections were performed at a current of 10 nA, accelerating voltage of 15 keV, and beam diameter of 10 μm to avoid destroying the hydrated serpentine sample to analyze the major element compositions of Si, Al, Mg, Na, Ca, Cr, K, Fe, Mn, and Ti, using natural standards.

Samples were reacted with 100% H_3PO_4 at 90 °C and then used for carbonate quantification, along with carbon and oxygen isotope analyses ($\delta^{13}C$ and $\delta^{18}O$), which were

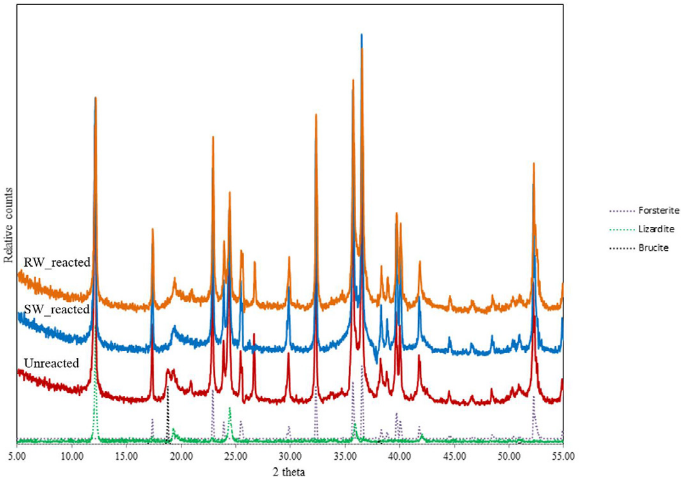

Fig. 2. Powder XRD of unreacted and reacted Oman dunite with SW and RW media. Unreacted rock (red) contains lizardite (green dashed, RRUFFID = 60006), forsterite (purple dashed, RRUFFID = 100099), and brucite (black dashed, RRUFFID = 050455). Lizardite and forsterite are in the SW reacted rock (blue) and RW reacted rock (orange), but brucite is no longer present. The main magnetite peak overlaps forsterite at ~36 2 theta, thus it is hard to identify magnetite with powder XRD. (For interpretation of the references to color in this figure legend, the reader is referred to the web version of this article.)

Table 4
Quantitative powder XRD measurements determined by RockJock of unreacted Oman dunite.

Mineral	Unreacted Oman dunite	
	wt%	Normalized wt%
Forsterite	53	51
Brucite	6	6
Serpentine (Chrysotile + Lizardite)	46	43
Total	105	100
Full pattern degree of fit	0.1393	

determined using a GV IsoPrime mass spectrometer with Dual-Inlet and MultiCarb systems in the Center for Stable Isotope Biogeochemistry (CSIB) at Department of Integrative Biology, University of California at Berkeley. Several replicates of one international standard NBS19, and two lab standards $CaCO_3$-I & II were measured along with samples for each run. The overall external analytical precision is about ±0.05‰ for $\delta^{13}C$ and about ±0.07‰ for $\delta^{18}O$.

Total organic carbon (TOC) analysis was conducted in the Kiowa laboratory at University of Colorado at Boulder with a FLASH EA 1112 Series CHN analyzer, which consists of the system unit, a MAS 200 autosampler, and analysis with Eager 300 software.

3. RESULTS

3.1. Mineralogy and Fe-content of unreacted rock

The Oman dunite used in the water/rock experiments was extensively characterized to accurately quantify how the mineralogy and Fe speciation changed through the course of reaction at 100 °C. The mineralogy of our partially-serpentinized Oman dunite sample is dominated by olivine (51%), lizardite (43%), and brucite (6%); these peaks were identifiable with powder XRD (Fig. 2) and quantified using the USGS RockJock software (Table 4).

To further quantify mineralogy, as well as document its spatial relationships at the microscale, we employed two imaging techniques, QEMSCAN and Raman microspectroscopy. Spatially-resolved imaging (1 µm beam size at surface) with QEMSCAN of a ~13 mm by 23 mm heterogeneous area shows the complex structure of serpentine intermixed with olivine, and trace minerals: pyroxene, carbonate, Mg-Fe-Ca silicates, Mg-Ca carbonates, chlorite, and chromite (Fig. 3). Brucite was not detected with QEMSCAN. Raman hyperspectral maps verify the extensive presence of serpentine, specifically lizardite based off the shape and position of the OH peak near 3700 cm^{-1} (Rinaudo et al., 2003; Groppo et al., 2006; Petriglieri et al., 2015). In addition, Raman microspectroscopy reveals

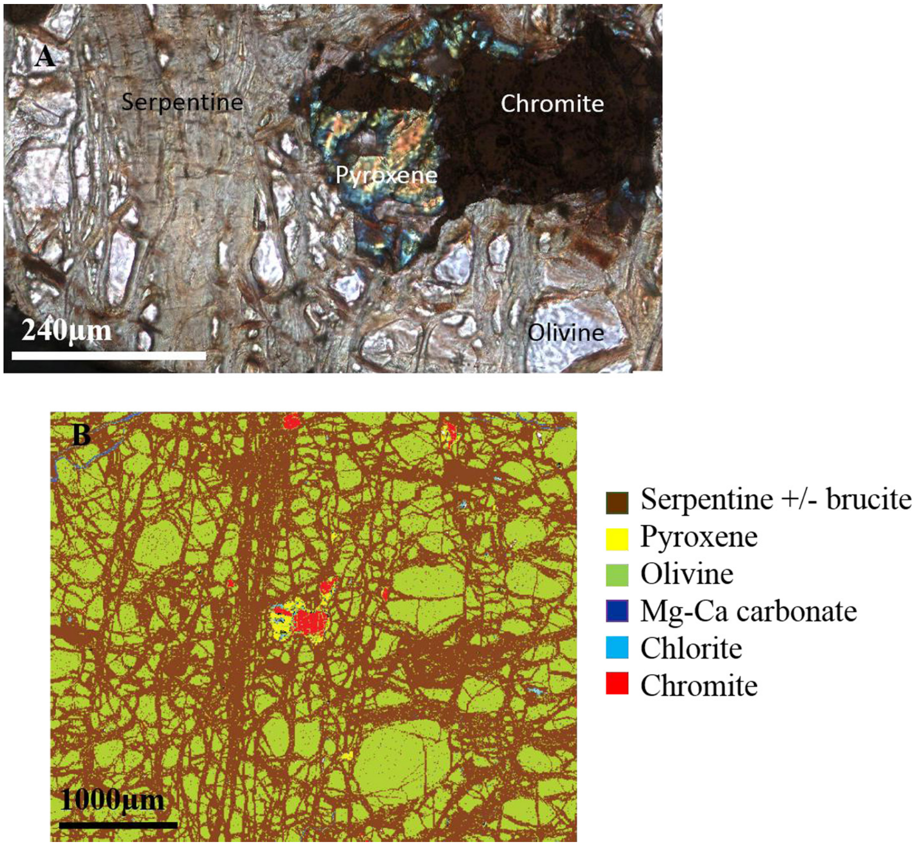

Fig. 3. (A) Transmitted light image of Oman dunite with key minerals labeled. (B) QEMSCAN image of grain mount of unreacted Oman dunite. Serpentine ±brucite (dark brown) encompasses ~50% of thin section, while other ~50% of minerals detected include olivine (light green), pyroxene (yellow), chromite (red), chlorite (dark green), Mg-Fe-Ca silicates (light blue) and unidentified Mg-Ca carbonates (purple). (For interpretation of the references to color in this figure legend, the reader is referred to the web version of this article.)

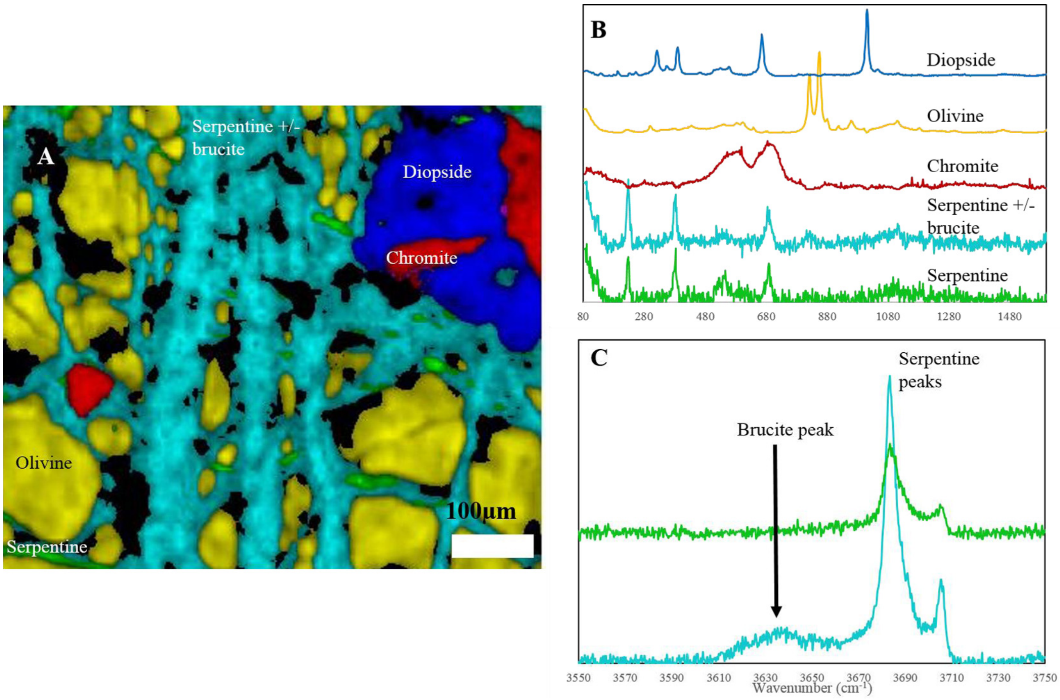

Fig. 4. (A) Hyperspectral MicroRaman map of Oman partially serpentinized dunite. Olivine (yellow) grains are surrounded by serpentine intermixed with brucite (cyan) and some serpentine with no brucite (green). There is a large chromite grain in the right corner (red), along with diopside (blue). Black regions indicate serpentine spectra intermixed with an epoxy signal. (B) Spectra in fingerprint region (80–1600 cm^{-1}) corresponding to colors on map. (C) OH stretch region for hydrous minerals in the map. The serpentine peaks are evident at 3680 and 3700 cm^{-1}, whereas the brucite peak is present mixed with the serpentine in the cyan spectrum at 3640 cm^{-1} (see arrow). (For interpretation of the references to color in this figure legend, the reader is referred to the web version of this article.)

Table 5

Electron microprobe data from serpentine in Oman dunite prior to reaction and after reaction in SW medium. Columns represent 6 different analysis points. The Si/(Mg + Fe) ratio should be 0.67 for a pure serpentine.% Brucite is calculated from the following equation: Si/(Mg + Fe) ratio = $x^*(0) + (1 - x)^*(0.67)$, where 0 is the theoretical ratio of Si/(Mg + Fe) for pure brucite and 0.67 is the theoretical ratio of Si/(Mg + Fe) for pure serpentine. Large standard deviations reflect the variability of brucite abundance in serpentine.

							Average (standard deviation)
Unreacted serpentine areas from Oman dunite							
Na_2O	0.00	0.00	0.00	0.00	0.00	0.00	0 (0.00)
MgO	36.84	36.45	39.86	39.29	39.00	38.29	38.29 (1.26)
Al_2O_3	0.00	0.00	0.00	0.00	0.00	0.00	0 (0.00)
SiO_2	37.31	30.45	35.10	36.19	36.44	35.10	35.10 (2.22)
CaO	0.05	0.04	0.08	0.05	0.05	0.05	0.05 (0.02)
FeO	5.91	4.47	6.66	5.97	7.64	6.13	6.13 (0.95)
MnO	0.14	0.11	0.09	0.09	0.11	0.11	0.11 (0.02)
Total	80.25	71.51	81.79	81.59	83.24	79.68	79.68 (3.83)
SW Reacted serpentine areas							
Na_2O	0.00	0.04	0.00	0.04	0.04	0.00	0.02 (0.02)
MgO	38.87	37.61	37.13	37.74	36.41	40.51	38.05 (1.33)
Al_2O_3	0.00	0.00	0.00	0.00	0.00	0.00	0 (0.00)
SiO_2	41.16	39.27	39.24	39.83	38.43	35.81	38.96 (1.63)
CaO	0.00	0.08	0.08	0.07	0.07	0.07	0.06 (0.03)
FeO	4.33	5.42	6.57	4.38	8.48	6.21	5.90 (1.43)
MnO	0.00	0.10	0.00	0.00	0.16	0.12	0.06 (0.07)
Total	84.36	82.51	83.02	82.05	83.59	82.72	83.04 (0.75)

that serpentine is intimately intermixed with brucite, at a scale of <1 μm. Brucite can be clearly detected in the OH stretch region at 3640 cm^{-1} even though it is obscured by serpentine in the fingerprint region of 80–1600 cm^{-1}. Fig. 4 shows the intermixed serpentine and brucite spectra, along with a pure serpentine spectrum. Nearly all of the serpentine in the dunite contained this mixture of brucite and serpentine. Other discrete mineral phases detected include diopside, enstatite, magnetite, chromite, and olivine (Fig. 4). Confocal Raman spectroscopy was also used to look for fluid inclusions in mineral grains. We found small (~1 μm) magnetite grains inside some olivine grains, but no evidence of H_2 or CH_4 bearing fluids. The dunite contains 0.24% carbonate, as measured by the amount of CO_2 evolved from acidification, which is approximately 0.012 g of the total weight of the original 5 g sample (Supplementary Table 2).

Electron microprobe analyses were used to determine the composition of the olivine grains and infer the chemical composition of the serpentine/brucite mixtures in Oman dunite. The average olivine formula in the Oman dunite sample is $(Mg_{1.80}Fe_{0.20})SiO_4$. The Fe concentration in the serpentine/brucite varied from 4.47 to 7.64 wt% FeO (Table 5) and the weight percent oxide totals were low (71–84 wt%). These total weight percent oxide values fall between predicted total weight percent oxide for serpentine (87%) and brucite (69%) due to intermixing of these phases. However, this particular technique is likely overestimating the amount of brucite mixed with serpentine as multiple other techniques do not detect brucite after reaction (Supplementary Text 1).

We estimated the Fe-content of the brucite to be 18 wt% FeO using Raman spectroscopy. The Fe-content was calculated by determining the position of the OH peak of the brucite spectrum near 3650 cm^{-1}. This peak shifts to lower wavenumbers when Fe substitutes into brucite (Reynard et al., 2015). We prepared a calibration from a suite of 20 natural and synthetic brucites with a range of iron concentrations that showed the position of the OH peak decreases by ~0.9 cm^{-1} per wt% FeO. This slope was used to calculate the 18 wt% FeO in our brucite, or in terms of wt% MgO, 53, with a Mg # of 0.86.

Table 6
Concentrations of H_2 in water/rock reactions when reacting with artificial sulfate-free seawater (SW) media, presented in terms of total amount H_2 per reaction (nmol), amount normalized to mineral mass (nmol/g), and aqueous H_2 concentration (nM) for convenience. Significant figures reflect an uncertainty of 5% in the original H_2 headspace measurement by GC in μmol/mL. SW_C1 and SW_C2 are control vials without minerals. Blanks are in duplicate and reactions in triplicate.

Day	SW_C1	SW_C2	SW_1	SW_2	SW_3
Total H_2 in fluid and headspace (nmol)					
0	0	0	0	0	0
2	0	0	87	73	69
48	48	38	850	850	920
92	190	200	2400	2000	2000
203	180	80	1500	1400	1550
Total H_2 in fluid and headspace (nmol/g mineral)					
0	0	0	0	0	0
2	0	0	17	15	14
48	10	8	170	170	180
92	38	41	470	400	400
203	36	16	310	270	310
H_2 in fluid (nM)					
0	0	0	0	0	0
2	0	0	46	39	37
48	39	35	740	570	610
92	100	100	1300	1100	1100
203	96	43	810	720	820

We quantified the oxidation state of Fe-bearing minerals in the unreacted and reacted rock powders because Fe-oxidation drives hydrogen production during

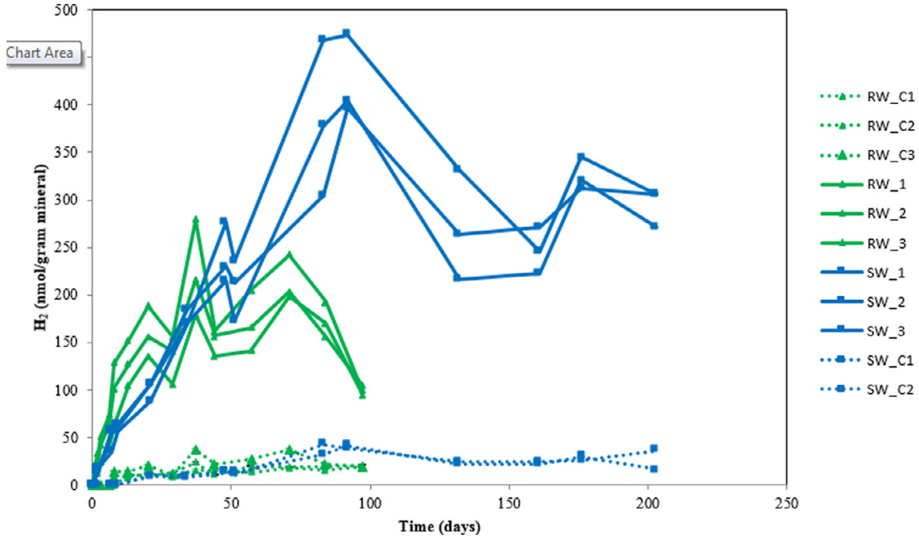

Fig. 5. Hydrogen production at 100 °C from reaction of partially serpentinized Oman dunite with SW media (blue lines) and Oman RW media (green lines), conducted in triplicate. Controls (vials filled with fluids, no minerals, purged with N_2:CO_2) are shown with dashed lines, respectively. Net H_2 concentrations increase for 50–100 days and then decrease. (For interpretation of the references to color in this figure legend, the reader is referred to the web version of this article.)

Table 7
Concentrations of H_2 in water/rock reactions when reacting with artificial rainwater (RW) media presented in terms of total amount H_2 per reaction (nmol), amount normalized to mineral mass (nmol/g), and aqueous H_2 concentration (nM) for convenience. Significant figures reflect an uncertainty of 5% in the original H_2 headspace measurement by GC in μmol/mL. RW_C1, RW_C2, and RW_C3 are control vials without minerals.

Day	RW_C1	RW_C2	RW_C3	RW_1	RW_2	RW_3
Total H_2 in fluid and headspace (nmol)						
0	0	0	0	0	0	0
2	0	0	0	59	130	170
13	35	52	73	530	630	760
37	76	110	180	900	1100	1400
97	94	100	94	480	530	500
Total H_2 in fluid and headspace (nmol/g mineral)						
0	0	0	0	0	0	0
2	0	0	0	12	26	34
13	7	10	15	110	130	150
37	15	23	37	180	220	280
97	19	21	19	96	110	100
Total H_2 in fluid (nM)						
0	0	0	0	0	0	0
2	0	0	0	31	70	90
13	19	28	39	280	340	400
37	41	61	98	480	580	740
97	50	55	50	250	280	270

serpentinization. Pre-edge multiple energy mapping of serpentine and brucite in a thin section of Oman dunite was conducted at BL2-3 at SSRL to determine Fe^{3+}/Fe_{Total} prior to laboratory water/rock reaction. Following the work of Wilke et al. (2001) and Andreani et al. (2013), the range of pre-edge centroids and intensities of unreacted serpentine and brucite XANES were plotted on a Fe variogram to quantify the Fe(II)/(III) ratios (Supplementary Fig. 2). The Fe(III) content of intermixed serpentine and brucite ranged from ∼40% to 80% of the total Fe in each analysis (error of ±10%).

3.2. Hydrogen production

Both SW and RW water/rock reactions begin making small amounts (12–34 nmol/mineral) of hydrogen after reacting for 2 days (Tables 6 and 7 and Fig. 5). The reaction with SW media produced the highest measured total H_2 concentrations (summed from both the fluid and the headspace) of 470 nmol/g mineral after 92 days of reaction. Hydrogen is partitioned into different reservoirs (headspace vs. aqueous phase), and thus we report the concentrations of H_2 in nmol in fluid and headspace, nmol (total in fluid and headspace)/g mineral, and nM in fluid (Tables 6 and 7). The H_2 in the SW experiment decreased to 270–310 nmol H_2/g mineral after 203 days (Table 6 and Fig. 5). The RW media also produced significant H_2, with peak concentrations at 37 days with a maximum 280 nmol H_2/g mineral (Table 7). H_2 concentrations in RW media then decreased to 96–110 nmol H_2/g mineral at 97 days (Table 7 and Fig. 5).

Control vials with RW or SW solutions equilibrated with $N_2:CO_2$ were also regularly analyzed, since incubating silica serum vials with fluids and butyl stoppers produces small amounts of H_2 (Mayhew et al., 2013; McCollom and Donaldson, 2016). In these experiments, the controls all exhibit H_2 concentrations of 200 nmol or less in the fluid plus headspace throughout the lifetime of the experiment. Although this pathway for generation of small amounts of hydrogen complicates calculations of the amount of H_2 generation by reaction of aqueous fluids with minerals from the Oman dunite sample, the effect is minimal because the observed concentrations of H_2 from the 100 °C reactions are an order of magnitude higher than the concentrations of H_2 in the controls.

3.3. Aqueous chemistry

Within 24 h of the onset of the reaction at 100 °C, the pH increases from ∼5–6.5 to 8.5–9 in both SW and RW media, and then decreases slightly to 8–8.5 for the lifetime of the experiments (Supplementary Fig. 3). As discussed in methods, these values reflect the pH measured at 25 °C, not the in situ pH values, which are expected to be 1–2 pH units lower. The headspace CO_2 concentration decreases over time in both media. Unfortunately, the initial headspace CO_2 concentration in the water/rock reactions was not measured, but we did measure the headspace CO_2 concentration in the control vials after 171 days (RW) and 304 days (SW). As the control vials are non-reactive, this headspace CO_2 concentration approximates the initial headspace CO_2 concentration in the vials with rock. From this assumption, the $CO_{2(aq)}$ concentrations in the RW experiments begin at ∼7.0 μmol/mL and decreased to ∼1.0 μmol/mL after 6 months. The $CO_{2(aq)}$ concentrations in the SW experiments start at ∼4.0 μmol/mL and decreased to ∼0.03 μmol/mL after 10 months. No CH_4 was detected in any of the vials with a gas chromatograph detection limit of ∼10 nmol.

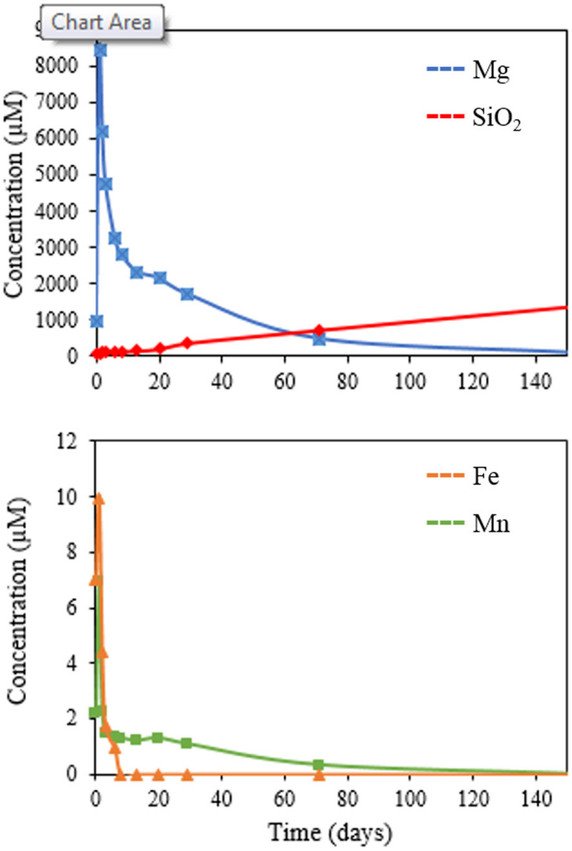

Fig. 6. Water chemistry of RW media reacting with Oman dunite over 50 day period; later time points were not included because concentrations do not vary significantly after 50 days. Initial release of Mg^{2+}, Fe^{2+}, and Mn^{2+} results in maximum cation concentrations after 24 h of reaction, then levels decline over time. Release of $SiO_{2(aq)}$ is not detected in the first 10 days, but $SiO_{2(aq)}$ does slowly increase over the course of the experiment. Other major cations, anions, and trace metals (Ca^{2+}, Ni, Cr, SO_4^{2-}) were measured but did not change significantly with time.

The final aqueous geochemistry measurement was on day 155 for RW experiments and day 287 for SW experiments. In addition, samples were also analyzed from early time-points in the RW media experiment. The composition of the reacted fluid was measured after 24 h of reaction and showed a rapid increase in the concentration of Mg^{2+}, Fe^{2+} and Mn^{2+} ions in solution. Then, concentrations of Fe^{2+} and Mn^{2+} decreased rapidly to near initial concentrations, while Mg^{2+} decreased more gradually over time (Fig. 6). Silica gradually increased over time. Most of the increase concentration of silica is due to the dissolution of the silica serum vials, as seen by similar silica concentrations in control and water/rock vials (Supplementary Table 1). The aqueous chemistry of the SW experiments was not measured at early time points.

3.4. Low molecular weight organic acids

Dissolved low molecular weight organic acids were measured in the water/rock reactions and controls (Table 8). The fluids were extracted from the experiments after decreases in the H_2 headspace concentration were observed, on day 525 for SW and 392 for RW. 40.2–98.1 μM of formate and 38.2–91.2 μM of acetate were observed in the RW and SW experiments. Less than 13.5 μM of propionate, butyrate, valerate, and lactate were detected in the products of the SW and RW experiments (Table 8). We believe the control experiments have small amounts of organic acids due to contamination from the butyl rubber stoppers. Organic acid concentrations in the water/rock experiments are significantly higher than in mineral-free controls (Table 6). Thus, we infer that formate and acetate were generated in the SW and RW water/rock reactions as H_2 and CO_2 were consumed. Formate was more abundant in the RW experiments while acetate was more abundant in the SW experiments.

To confirm that CO_2 was required to generate organic acids, separate SW- and RW-dunite experiments were conducted with only N_2 in the headspace (see Fig. 1). These experiments serve as controls because without CO_2 in the headspace, there is little carbon to react with H_2 to make low molecular weight organic acids. SW and RW media do contain small amounts of HCO_3^-, 2.41 and 0.02 mM, respectively. However, this carbon does not appear to transform into organic acids. The N_2-only reactions generated similar levels of H_2 to the SW and RW reactions, but contained much lower concentrations of organic acids, similar to the controls with no minerals. These experiments were not run in triplicate, so their H_2 generation results are not reported. They contained <13.1 μM formate, <18.5 μM acetate, and <1.5 μM lactate, propionate, butyrate, and valerate, confirming that the elevated levels of organic acids are only observed when dissolved CO_2 is provided as a reactant.

3.5. Mineralogy and Fe-content of reacted rock

Minerals were sampled from the RW and SW experiments one or more times after extensive water/rock reaction; the exact sampling times are detailed in Table 3. A secondary, white mineral precipitate formed during both the SW and RW water/rock reaction after ~30 days of reaction. Several techniques were used to try to quantify the mineralogy and Fe-content of this mineral. Secondary precipitate was collected from SW media after ~90 days of reaction to analyze with powder XRD. The diffraction peaks most closely align with lizardite (Fig. 7). However, olivine peaks were also present, showing that the secondary mineral was not fully separated from the primary olivine. There was not sufficient material available to conduct powder XRD on the secondary mineral formed in the RW medium. Raman spectra of single grains of the secondary mineral in both samples (SW_reacted and RW_reacted) fit the spectrum of serpentine (Fig. 8). The serpentine created during the water/rock reactions is clearly visible in grain mounts of reacted SW and RW minerals, which also demonstrate that serpentine and olivine are the dominant minerals (Fig. 9). Scanning electron microscopy was used to image the newly-formed serpentine and acquire EDS spectra for both the SW and RW reacted grains (Supplementary Fig. 4). The serpentine is variably platy and globular, coating olivine grains. Electron dispersive spectroscopy data indicate that the serpentine contains Mg, Si, and O with trace amounts of Al and Fe (Supplementary Fig. 4). The presence of carbon cannot be assessed because both samples were carbon coated. However, no carbonate formation was observed by probing the grains with Raman spectroscopy, powder XRD, and SEM. We analyzed the reacted SW and RW grains with a mass spectrometer to quantify any trace carbonate formation, but the amount of CO_2 evolved from acidification of the samples was less than or equal to that of the unreacted dunite (Supplementary Table 2). We also analyzed the grains for total organic carbon (TOC) by combustion techniques, but all organic carbon values were less than the lowest standard run (0.109 mg of 70% carbon); the organic carbon is not quantifiable by this technique for our samples.

The average surface area of the mineral grains increased by more than an order of magnitude during the course of the reactions, which is attributed to the formation of the amorphous serpentine. The unreacted rock had a surface area of 0.47–0.60 m^2/g. After reaction with RW, average surface area increased to 6.31 m^2/g, while the average surface area of the mineral grains reacted with SW increased to 10.17 m^2/g. The length of olivine grains in unreacted and reacted grains was measured (Supplementary Table 3), and did not change throughout the experiment. Thus, the surface area increase is due to the precipitation of new serpentine and not to the fragmentation of existing olivine.

Changes in magnetic susceptibility were quantified for the rock reacting in the RW media. The results show an increase in magnetite content after water/rock reaction. Both the unreacted and reacted dunite powders are paramagnetic; they only demonstrate magnetic properties in the presence of an applied magnetic field. The remanent magnetization (residual magnetism remaining after external magnetic field is removed) in the unreacted rock is 0.1353 $A{\cdot}m^2$ (emu), whereas the remanent magnetization in the reacted rock is 0.1828 $A{\cdot}m^2$ (emu). The saturation magnetization is 0.0036 $A{\cdot}m^2$ (emu) for the unreacted rock and 0.0101 $A{\cdot}m^2$ (emu) for the reacted rock (Table 9).

Notably, brucite was not present in the Oman dunite samples after reaction with SW and RW. Powder XRD reveals a brucite peak at 18.8 2θ in unreacted rock that is no longer present in the SW and RW reacted products. The lack of brucite in the reaction products was confirmed by analyzing the reacted grains with Raman spectroscopy and noting the absence of the brucite OH stretch at $\sim$3640 cm^{-1} from both SW and RW media after >1 year of reaction. In contrast, brucite is pervasive in the unreacted mineral grains (Fig. 4).

Electron microprobe was used to quantify the % FeO concentration in the olivine and serpentine from the SW experiments to determine any changes during the reaction (Table 5). The SW reacted olivine FeO values were similar to the unreacted olivine at $\sim$10 wt% FeO. A range of 4.33–8.48 wt% FeO in serpentine was observed, similar to the unreacted serpentine.

The bulk iron speciation of the dunite was also assessed before and after reaction using Fe K-edge XANES spectroscopy. Least squares fitting of bulk XANES spectra was employed to show that the Fe speciation of the XANES spectra from both the unreacted dunite and the reaction products from the RW experiments can be fit using approximately 50% serpentine and 50% olivine, with a sensitivity of ±10%. There was no discernible shift in the overall Fe XANES spectrum for the unreacted and reacted rock (Supplementary Fig. 5). In addition, Fe pre-edge XANES analyses were conducted at the microscale for the newly-formed serpentine in RW experiments to determine the Fe(III)/Fe_T ratio. These measurements were challenging because the newly-formed serpentine contains low iron concentrations. For the spectra obtained, the centroids and intensities of the pre-edge spectra were plotted in the Fe(III)/Fe_T variogram (Supplementary Fig. 2) and compared to the range of Fe(III)/Fe_T ratios found in serpentine from unreacted Oman dunite obtained from a multiple energy pre-edge map (Wilke et al., 2001; Mayhew et al., 2013; Muñoz et al., 2013; Andreani et al., 2013). Some newly-formed serpentine falls within the range of pre-existing serpentine Fe(III)/Fe_T ratios, which vary from 40% to 80% Fe(III)/Fe_T. However, some spot analyses show >90% Fe(III), which is more oxidized than any of the pre-existing serpentine. Unfortunately, we could not conduct the same analysis on the newly-formed serpentine in SW media because it was difficult to separate it from grains of olivine.

3.6. Mass balance of Fe during the water/rock reactions

TGA analysis of the minerals from the unreacted and reacted RW experiments was used to quantify changes in the total mass of serpentine and brucite during water/rock reaction. The TGA data for the unreacted Oman dunite indicated that brucite made up $\sim$5 wt% of the initial mineralogy, and serpentine was 38 wt% of the unreacted rock (Fig. 10). After the RW reactions, serpentine remained 38 wt% of the mineralogy, while brucite was not detected. We have reservations about TGA analysis because we have tested how well TGA can estimate a known mixture of brucite and serpentine, and the analysis underestimated the amount of brucite and overestimated the amount of serpentine (explained in detail in Miller et al. (2016)). Despite these reservations, the TGA data affirms the presence of both brucite and serpentine in the unreacted rock. It also shows that brucite is not present in the reacted product and provides an approximation of mass change during water/rock reaction.

Bulk powder XRD measurements show the loss of the brucite peak at 18.8 2θ for both RW and SW reacted grains (Fig. 2). The dominant olivine and serpentine peaks were similar pre- and post-reaction. The initial mineralogy of Oman dunite was quantified using the USGS RockJock software. The results from this technique are consistent with TGA results: 44% serpentine, 6% brucite, and 46% forsterite (Table 4). Quantification of SW and RW reacted grains was attempted with RockJock, but reasonable data were not obtained because the amount of olivine present appeared to increase after water/rock reaction. This likely indicates that a representative sample was not used, perhaps due to the abundance of amorphous precipitated serpentine that did not homogenize well with the more durable olivine grains. However, the brucite peak disappears in the

Table 8
Organic acid measurements (μM) of 100 °C water/rock reactions. C indicates "control" vials with no minerals present, and N_2 indicates vials purged with only N_2 gas, whereas all the others were purged with $N_2:CO_2$. ND indicates no detection, while BDL indicates below the limit of detection, but a signal is still present. The results are highlighted with bold text. SW fluids were sampled after 525 days of reaction and RW fluids after 392 days of reaction with $N_2:CO_2$. N_2-only purged samples were measured after 308 days of reaction. The low concentrations of propionate, butyrate, lactate, and valerate are not statistically significant.

Sample	Formate	Acetate	Lactate	Propionate	Butyrate	Valerate
Limit of detection (μM)	3.3	5.1	1.8	0.1	4.1	0.3
SW_C1	21.9	15.4	ND	10.4	ND	ND
SW_C2	18.4	12.9	ND	13.5	ND	ND
SW_1	**40.2**	**81.7**	**BDL**	**11.8**	**ND**	**ND**
SW_2	**57.4**	**50.4**	**BDL**	**13.6**	**ND**	**1.7**
SW_3	**52.9**	**69.9**	**ND**	**12.1**	**ND**	**1.5**
RW_C1	19.0	7.6	ND	0.2	BDL	ND
RW_C2	57.5	7.6	ND	0.4	ND	ND
RW_C3	54.1	12.2	ND	0.3	ND	0.9
RW_1	**98.1**	**38.8**	**ND**	**0.8**	**ND**	**1.4**
RW_2	**73.4**	**38.2**	**ND**	**0.6**	**BDL**	**ND**
RW_3	**82.5**	**91.2**	**ND**	**1.1**	**ND**	**0.4**
SW_N2	13.1	18.5	BDL	1.5	ND	ND
RW_N2	7.7	16.3	BDL	1.5	ND	ND

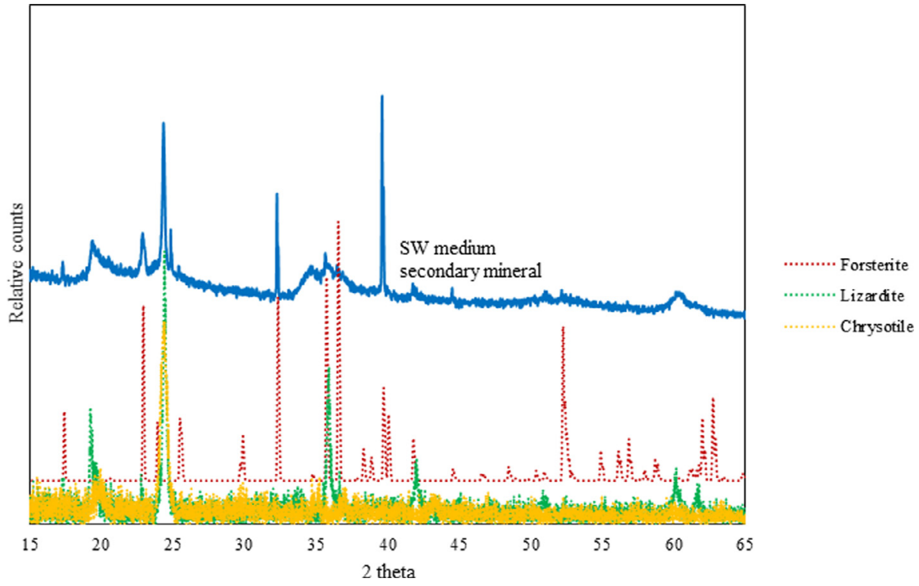

Fig. 7. Powder XRD spectrum of secondary mineral (blue) that forms in SW medium reaction. The spectrum fits most strongly to lizardite (green dashed), but also has traces of olivine (red dashed) due to difficulty in completely separating the grains. Chrysotile (yellow dashed) was added to show the spectrum more closely fits lizardite. (For interpretation of the references to color in this figure legend, the reader is referred to the web version of this article.)

RW and SW bulk powders. This is consistent with corresponding data collected from Raman spectroscopy and TGA thus, it is reasonable to conclude that brucite was entirely consumed during water/rock reactions.

The maximum mass of magnetite generated during the RW water/rock reaction was calculated using a proportionality constant of 92 A·m^2/kg to empirically correlate the saturation magnetization to the amount of magnetite using the methods of Malvoisin et al. (2012a,b). This calculation yields a total of 1.1 mg of magnetite in unreacted Oman dunite and 2.7 mg of magnetite after reaction in RW media, per 5 g of dunite reacted. Thus a maximum of 1.6 mg of magnetite was produced, which is equivalent to 0.31 mmol of magnetite. This estimate assumes the sole magnetic carrier in the sample is magnetite, which may not be true due to the prevalence of Fe(II & III)-bearing serpentine. Also, it is possible that maghemite formed, which oftentimes forms when magnetite is oxidized at low-temperatures (Oufi et al., 2002). The powder XRD peaks of the two minerals overlap (Kim et al., 2012) and XANES spectra are also similar (Espinosa et al., 2012), thus it is difficult to certainly state the mineral product. Maghemite has a proportionality constant of 65.3 A·m^2/kg (Özdemir and Dunlop, 2010), which would correspond to 1.6 mg of maghemite in unreacted Oman dunite and 3.8 mg of maghemite formed in RW vials. This is discussed in more detail later.

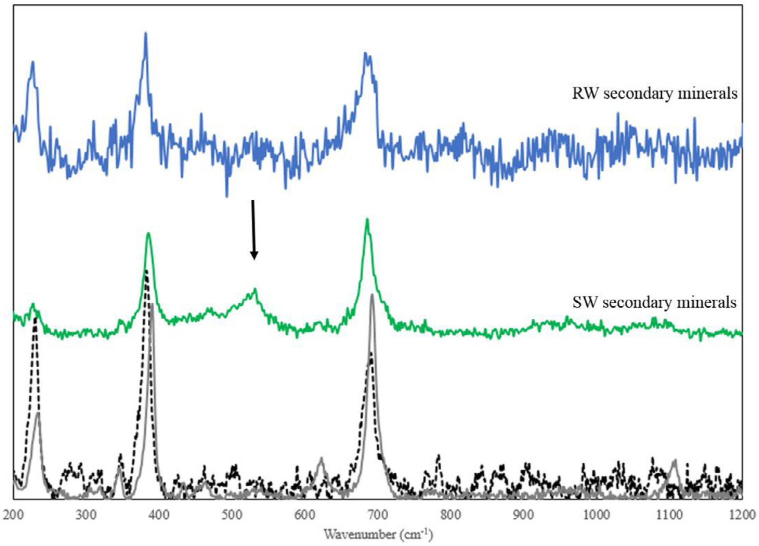

Fig. 8. Raman spectra of SW secondary minerals (green) and RW secondary minerals (blue) compared to a lizardite Raman spectrum (black dashed, RRUFFID = R060006) and chrysotile Raman spectrum (gray, RRUFFID = R070088). Secondary minerals are not fully crystalline, thus do not produce high signal to noise spectra. The black arrows above the small peak at 550 cm^{-1} (black arrow) in green is a common occurrence in serpentine from Oman; however, the exact chemical composition leading to that peak is unclear. (For interpretation of the references to color in this figure legend, the reader is referred to the web version of this article.)

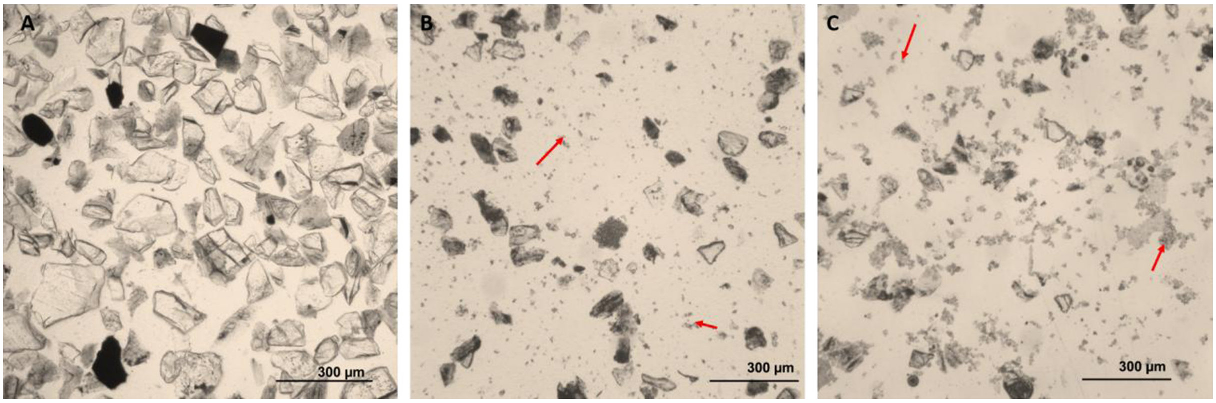

Fig. 9. Image of unreacted Oman dunite grain mount (A) with clear olivine, serpentine, and opaque chromites. The serpentine was extracted with a 23 gauge needle from the anaerobic serum vials, along with other fine-grained particles from RW reacted (B) and SW reacted (C) experiments and mounted on grain mounts. The amorphous serpentine can be seen dispersed throughout the epoxy (see red arrows), along with clear olivine grains and dark serpentine grains. (For interpretation of the references to color in this figure legend, the reader is referred to the web version of this article.)

Table 9
Magnetic susceptibility measurements for powdered Oman dunite, before and after water/rock reaction with rainwater (RW) media.

Sample	Magnetic type	Remanent magnetization (Mr) (A·m^2/emu)	Saturation magnetization (Ms) (A·m^2/emu)	Coercivity (Hc)
RW_unreacted	Paramagnetic	0.1353	0.0036	116.6438
RW_reacted	Paramagnetic	0.1828	0.0101	108.9219

4. DISCUSSION

4.1. Hydrogen production at 100 °C

Our experimental low-temperature water/rock reactions with Oman dunite produce sufficient hydrogen over prolonged time-scales to sustain subsurface microbial activity. Methanogens grow in a variety of environments with low levels of hydrogen comparable to this study, with dissolved aqueous concentration of up to 1.3 μM H_2 at pH ~ 9: rice paddies (28 nM H_2), lake sediment (36 nM H_2), sewage sludge (203 nM H_2), and hot springs

(>300 nM H_2) (Zinder, 1993; Spear et al., 2005). Other hydrogenotrophic anaerobes, such as *Desulfovibrio* and *Acetobacterium*, require even less H_2 (<10 nM H_2) to sustain growth (Zinder, 1993).

Partially serpentinized dunite has the capability to produce large quantities of H_2, even when the primary olivine and pyroxene are already partially serpentinized. The experiments described herein gave rise to some of the highest concentrations reported in the literature for H_2 generated at low-temperatures (Table 1). A maximum of 470 nmol H_2/g mineral was measured after several months of water/rock reaction at 100 °C in SW media. However, the maximum hydrogen generated is likely greater than the reported value because we did not correct for the H_2 removed from the headspace during sampling. Comparable amounts of H_2, up to 500 nmol/g H_2, were produced by reaction of Snake River Plain basalt at 22 °C at a pH of 6 (Anderson et al., 1998). However, when the pH was increased to 8 in subsequent experiments, a more environmentally realistic condition that is also more similar to this study, the basalt did not dissolve and no H_2 was detected. Previous studies conducted with variably altered dunite from the Leka ophiolite produced up to 110 nmol/g H_2, which was particularly notable given the low reaction temperature of 25 °C (Okland et al., 2012). Our work also uses partially serpentinized dunite, but at higher reaction temperatures. Under these conditions, we generated more H_2 than recent experiments on the hydration of individual Fe (II)-bearing rocks and minerals, such as olivine, pyroxene, magnetite, as well as fresh San Carlos peridotite where a maximum of 300 nmol/g mineral H_2 was observed at 100 °C (Mayhew et al., 2013).

We believe the rapid increase in pH, concurrent with cation release, is due to brucite dissolution. The RW vials have a notable spike in Mg^{2+}, Fe^{2+}, and Mn^{2+} after 24 h of reaction (Fig. 6), that is attributed to the dissolution of (Mg, Fe) brucite containing small amounts of Mn^{2+}. The concentration of these cations decreases after the initial dissolution of brucite, possibly because the cations are incorporated into newly crystallized magnetite, serpentine, or trace secondary phases. There is no evidence of increased silica due to dissolution of any silicate phase.

Fluid composition exerts a strong influence on the extent of H_2 production. Reactions in SW produced more H_2 compared to reactions in RW media. Phosphate and bicarbonate are inorganic ligands in the SW media that can promote brucite dissolution by attacking surface metal-oxygen bonds (Pokrovsky et al., 2005). Additionally, the presence of Ca^{2+} in SW media (0.01 M Ca^{2+} in SW media versus 0.0005 M Ca^{2+} in RW media) may have led to increased brucite dissolution as inferred from experiments where the addition of 0.01 M Ca^{2+} to a brucite suspension resulted in an increase in brucite dissolution at pH 4.9 (Pokrovsky et al., 2005). The simulated SW is a higher ionic strength

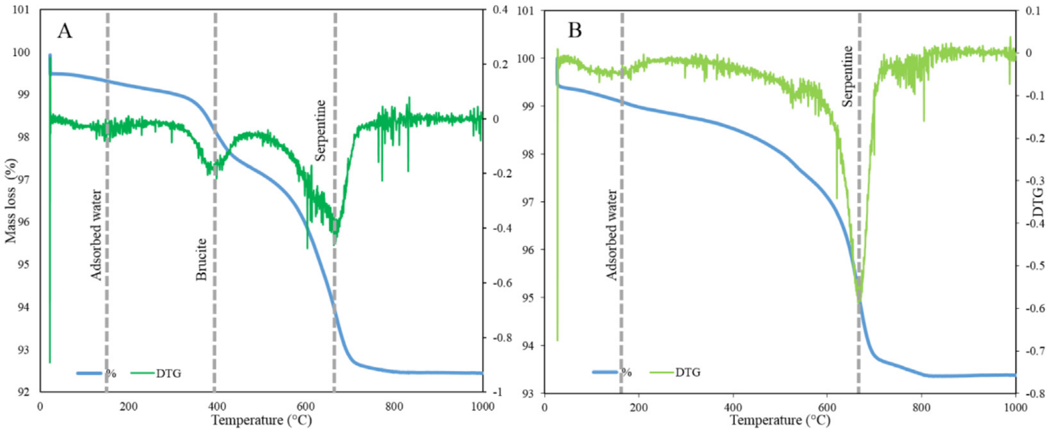

C.

Unreacted Oman dunite	mass % OH lost as measured by TGA	% mass of mineral in total rock
Brucite	1.7	5%
Chrysotile	4.9	38%
RW reacted Oman dunite		
Brucite	0.0	0%
Chrysotile	6.6	38%

Fig. 10. (A) TGA of unreacted Oman dunite shows brucite and serpentine present. (B) TGA of RW reacted dunite shows the absence of brucite peak and presence of larger serpentine peak. (C) Quantification of mass % brucite and mass % serpentine for unreacted dunite and RW reacted dunite derived from TGA.

media (0.73 M) versus RW media (0.005 M). However, dissolution rates of brucite, the key mineral releasing Fe(II) for oxidation, are not dependent on ionic strength, likely due to the double-layered brucite sheets that can accommodate high charge densities (Pokrovsky and Schott, 2004). In summary, a combination of increased inorganic ligands and divalent cations in SW vs. RW media appears to have caused faster rates of brucite dissolution in SW, affecting Fe(II) release and subsequent hydrogen generation.

4.2. Mineralogical changes during water/rock reaction

We investigated the changes between the initial and final mineralogy of the Oman dunite sample to determine which mineral/water reactions contribute to low-temperature hydrogen production. The unreacted and reacted rock powders were characterized by bulk powder XRD, Raman spectroscopy, TGA, chemical separation and magnetic susceptibility measurements to quantify mass balance (Table 3).

Mass balance calculations show that oxidation of only ~0.001% of the total Fe(II) in the dunite is required to explain the observed levels of H_2 production (Supplementary Table 4). It is very difficult to document such a small change. In addition, the water/rock reactions do not go to completion, nor are the minerals and aqueous solutions in equilibrium with each other. Thus, mineral analyses are dominated by the unreacted starting mineralogy. Any changes are likely on the order of milligrams of material that are heterogeneously distributed throughout the sample. Thus, we found it challenging to robustly quantify the small reservoirs of Fe(II) and Fe(III) that undergo a net change in these reactions. However, the combined suite of analytical techniques that we utilized did provide direct evidence for some changes in mineralogy and allowed us to estimate changes in modal abundance or chemical composition to partially constrain low-temperature serpentinization and H_2 production pathways.

The Oman dunite used for these experiments had already undergone at least one episode of serpentinization. The Fe-bearing phases in the partially serpentinized dunite are dominated by Fe(II)-bearing olivine, Fe(II) & Fe(III)-bearing serpentine, and Fe(II)-rich brucite, along with trace amounts of pyroxene, chromite, and magnetite. The serpentine and brucite are intimate mixtures presumably formed while the ophiolite was exposed to hydrothermal fluids at the mid-ocean ridge or during the process of obduction onto the Arabian Peninsula (Coleman, 1981; Boudier et al., 2010; Hanghøj et al., 2010), or during low temperature subaerial alteration (Barnes et al., 1978; Neal and Stanger, 1983; Kelemen and Matter, 2008; Kelemen et al., 2011; Miller et al., 2016). Thus, the starting mineral assemblage in Oman dunite contains several reservoirs of Fe(II) that may lead to hydrogen production in addition to, or instead of, serpentinization of the remaining olivine.

We do not observe significant olivine dissolution at 100 °C during the experiments. However, the detection limit of powder XRD is approximately 5% by weight, so some olivine could have dissolved without detection. This observation is supported by the slow rates of olivine dissolution at low temperatures; example rates from prior studies include $1.68 \times 10^{-12}\ \text{mol cm}^{-2}\ \text{s}^{-1}$ at 120 °C and pH 8.33 (Prigiobbe et al., 2009) and $2.10 \times 10^{-12}\ \text{mol cm}^{-2}\ \text{s}^{-1}$ at 120 °C and pH 9.44 (Hänchen et al., 2006). Another potentially reactive reservoir of Fe(II) in the dunite is pyroxene. However, as for olivine, there is little evidence for pyroxene dissolution during the course of these water/rock reactions. Serpentine is another reservoir of both ferric and ferrous iron that may react with water, leading to hydrogen production. Thus, the oxidation of existing Fe(II,III)-bearing serpentine can lead to the precipitation of newly-formed serpentine more enriched in Fe(III). However, given the initial abundance of serpentine in these experiments, it is difficult to detect changes in abundance or bulk chemistry. The pre-existing serpentine in the Oman dunite contains up to 10 wt% FeO, and this Fe may be >50% Fe(III) (Supplementary Fig. 2). Therefore, based on the analyses we were able to conduct, it remains unclear if the pre-existing serpentine quantitatively changes Fe(II/III) ratios during the experiments. However, the white precipitate that formed during water/rock reactions is unequivocally new serpentine.

Another reservoir of Fe(II) in the starting mineral assemblage is Fe(II)-bearing brucite that is intermixed with the serpentine. The brucite contains approximately 18 wt% FeO, making it a viable source of Fe(II) in solution. Ferrous hydroxide substituted into the brucite structure can give rise to H_2 production by the following end-member reaction (McCollom and Bach, 2009):

$$3Fe(OH)_2 = Fe_3O_4 + H_2 + 2H_2O \tag{1}$$

which results in the formation of magnetite as the sole Fe(III)-bearing mineral associated with hydrogen production. Reactions dissolving Fe-brucite and producing magnetite, similar to reaction (1), are likely to be the main cause of H_2 generation in our experiments, although there are other Fe(II)-bearing minerals present in the unreacted mineral assemblage. Reaction (1) indicates the importance of Fe(II)-bearing brucite, and is consistent with the observed, significant consumption of brucite and production of magnetite during our experiments. Additional, possible reactions that consume the Fe-component in brucite could produce additional H_2 in combination with Fe-oxyhydroxides such as bernalite ($Fe(OH)_3$) and goethite (FeO(OH)), or in combination with Fe(III) bearing serpentine. These can be approximated, as:

$$2Fe(OH)_2 + 2H_2O = 2Fe(OH)_3 + H_2, \quad 2Fe(OH)_2 = 2FeO(OH) + H_2 \tag{2, 3}$$

$$2Fe(OH)_2 + Mg_2SiO_4 + H_2O = Mg_2Fe^{3+}SiFe^{3+}O_5(OH)_4 + H_2 \tag{4}$$

Three mineralogical changes were observed in the 100 °C water/rock reactions: the disappearance of Fe-bearing brucite, the production of magnetite, and the precipitation of new Fe(III)-bearing serpentine. The new amorphous serpentine probably accounts for the increase in surface area from the unreacted to reacted products. Energy dispersive spectroscopy analyses suggest that the newly formed serpentine has similar Fe-content to the unreacted serpentine, with a Mg:Fe ratio of 7.8:1–5.9:1 in the new serpentine versus an average of 5.7:1 in unreacted serpentine. However, the new serpentine estimate is only based on two measurements. Although we could not quantify the mass of new serpentine formed, it was a small fraction of the initial mass, likely less than 1%. Although it is probably not a substantial reservoir for Fe(II) or Fe(III), the newly-formed serpentine in RW media does contain up to 95% Fe(III) compared to the 40–80% Fe(III) in the initial serpentine in the unreacted Oman dunite (Supplementary Fig. 2). This observation of Fe(III)-bearing serpentine corresponds to observations of Fe(III)-rich serpentine in highly altered Oman serpentinites (Streit et al., 2012) and the hypothesis that Fe(III)-bearing serpentine forms in other low-temperature water/rock experiments (Neubeck et al., 2014).

The source of silica to precipitate new serpentine may be small amounts of olivine or pyroxene dissolution, or the dissolution of the borosilicate serum vials in which the experiments were conducted (Supplementary Fig. 1). The addition of silica from the serum vials may also have contributed to brucite dissolution in the reactions (Ogasawara et al., 2013), however, it is still a relevant aqueous species in serpentinizing environments (Jöns et al., 2010; Miller et al., 2016). The newly-precipitated serpentine provides proof that Fe(III)-rich serpentine forms at low temperatures. However, we cannot determine whether or not serpentine formation is an important source of hydrogen generation in these experiments.

4.3. Proposed pathway and mass-balance for H_2 generation

We propose that the destabilization of Fe(II)-bearing brucite and subsequent oxidation of aqueous Fe(II) to form magnetite drives H_2 production in our low temperature laboratory water/rock experiments. This aligns with previous work in recognizing the importance of dissolution of Fe-bearing species (Stevens and McKinley, 2000; Mayhew et al., 2013; Neubeck et al., 2014; Okland et al., 2014), but varies because dissolution of Fe-bearing brucite, rather than olivine, is the most important source of Fe(II). There are several alternative pathways of low-temperature hydrogen however, they do not seem likely to have been important in our experiments (e.g. formation of silica surface radicals through rock communition (Telling et al., 2015) but this process does not explain hydrogen production over the observed 3 month time period); H_2 within fluid inclusions released during mineral dissolution (e.g. Neubeck et al., 2011) however, fluid inclusions were not detected using confocal Raman spectroscopy).

To assess our hypothesis regarding brucite reactivity, we made a simple calculation to test whether the Fe(II) originally contained in brucite, $Mg_{0.86}Fe_{0.14}(OH)_2$, could account for the maximum H_2 produced in the SW water/rock reactions. Based on our estimate of brucite abundance and iron content (Supplementary Table 4), and the stoichiometric reaction (1), we estimate that 251 μmol of H_2 could be produced if this reaction went to completion. This maximum amount of H_2 is 2 orders of magnitude higher than the production of H_2 we observed, 2.4 μmol. It is possible that more H_2 was produced than observed, for example if H_2 consumption was concurrent with H_2 production as organic acids were made, or if H_2 diffusion out of the experimental vials was significant. However, the total organic acids would only require 1.9 μmol of H_2. Another possibility is that a large fraction of the Fe(II) released from the dissolution of brucite was not oxidized and instead was sequestered into a Fe(II & III)-bearing serpentine.

The estimated mass of magnetite generated, as inferred from magnetic susceptibility data, can also be used to estimate the total H_2 produced during 100 °C water/rock reactions. Assuming all of the iron oxidation involved in magnetite production led to H_2 production, the formation of 13 μmol of Fe^{3+} in magnetite indicates that 6.5 μmol of H_2 were produced in our water/rock reaction experiments. Our maximum H_2 measurements were slightly lower, 2.4 μmol of H_2 (Table 6). It is possible that maghemite, another Fe^{3+}-bearing spinel, formed instead of magnetite. We cannot confirm the mineralogy of the paramagnetic mineral in our sample. If we make the same calculation as above assuming maghemite is the Fe(III)-bearing end product instead of magnetite, using a maghemite proportionality constant of 65.3 $A \cdot m^2/kg$ (Özdemir and Dunlop, 2010), we estimate 62.6 μmol of H_2 would be produced. This is much larger than the amount of H_2 observed.

This discrepancy between measured and calculated H_2 values may be due to errors with measuring nanoscale magnetite and applying the proportionality constant used to calculate mass of magnetite generated based on saturation magnetization (Malvoisin et al., 2012a,b). The error may also come from the fact that this method assumes magnetite is the sole magnetic carrier in the sample and neglects the potential importance of magnetite-spinel solid solutions (Shibuya et al., 2015), maghemite, and Fe(II & III)-bearing serpentine (Coey et al., 1981; Elmaleh et al., 2012). Unfortunately, we do not have measurements of magnetization as a function of temperature, to determine the exact source of the paramagnetic contribution.

Calculations suggest the water/rock reactions did not consume all of the Fe present in brucite to make H_2. Hydrogen may have been consumed before it accumulated in the headspace gas. We do not consider hydrogen diffusion out of the experimental vials to be a significant sink because the timing and rates of hydrogen production and loss are well replicated in these RW and SW experiments. The magnetite mass estimates closely align with maximum H_2 measurements, but they do suggest larger H_2 production than we observe.

4.4. Fate of carbon in water/rock reactions

We find compelling evidence for the formation of low molecular weight organic acids, specifically formate and acetate during our experiments. We briefly address these observations because of the significance of the synthesis and accumulation of low molecular weight organic acids in serpentinizing systems as potential energy sources for microbial metabolisms (e.g. methanogens, sulfate reducers, and metal-reducers (Jetten et al., 1992; Zinder, 1993; McCollom and Seewald, 2001). Organic acids may be a carbon source for microbial biosynthesis when inorganic carbon is limiting under hyperalkaline conditions. Inorganic low weight molecular synthesis is possibly as an important process for the origin of life (Russell and Martin, 2004; Russell et al., 2010). Additionally, formate and acetate have been observed in many actively serpentinizing systems (e.g. (Lang et al., 2010; Morrill et al., 2014; Crespo-Medina et al., 2014; McDermott et al., 2015).

Headspace carbon dioxide, along with H_2, decreases significantly over the course of the water/rock reactions (Supplementary Table 5). Thus, it is feasible that the hydrogen is reacting with CO_2 to form low molecular weight organic acids via the following reaction (McCollom and Seewald, 2003):

$$HCO_3^- + H_2 = CHOO^- + H_2O \tag{5}$$

Eq. (5) is dependent on high concentrations of H_2, and a relatively alkaline pH (8–10) for HCO_3^- to be an important carbonate species in solution, conditions met by our experimental system. However, this reaction is only experimentally shown to equilibrate rapidly from 175 to 300 °C (McCollom and Seewald, 2001, 2003; Seewald et al., 2006), not at 100 °C as observed in our experiments.

The formation of acetate is more enigmatic. Modeling of acetate, propionate, and butyrate formation shows it is thermodynamically favored when cold, oxidized seawater rich in bicarbonate mixes with hot, reduced hydrothermal fluids (Shock and Schulte, 1998). Yet our batch water/rock reactions do not have a compositional gradient characterized by disequilibrium between two fluids thus we suggest that our tentative findings must be replicated and verified with a $NaH^{13}CO_3$ tracer (McCollom and Seewald, 2001) to investigate all possible sinks of carbon in the system.

The water/rock reactions produced insufficient H_2 to produce the concentrations of formate and acetate observed, thus we assume organic acid production was concurrent with H_2 generation. For example, Eq. (5) was used to calculate the theoretical amount of hydrogen needed to produce the ~50 μM of formate observed in our experiments in SW media, which is 1.75 μmol of H_2 in 35 mL of fluid. The maximum H_2 observed was 2.4 μmol at 92 days, which then decreased to 0.89 μmol at 203 days, for a total of 1.48 μmol of H_2 consumed. This is not enough H_2 to generate the 1.75 μmol of formate observed, and also does not provide enough reducing equivalents to make the 2.45 μmol of acetate observed. Instead, we assume that organic acid production was concurrent with H_2 generation. Our measurements of the hydrogen concentration in the headspace simply do not accurately capture all of the Fe(II)-oxidation occurring in the water/rock reactions, and may be an underestimate of ~2.7 μmol of H_2-equivalents if we consider formate and acetate as reaction products.

An alternative explanation would be that the observed organic acids were released from fluid inclusions that preserved products of earlier high-temperature serpentinization. However, we did not observe fluid inclusions in olivine, and significant olivine dissolution is not observed during the 100 °C reactions. Additionally, control experiments, with partially serpentinized Oman dunite, SW and/or RW media, only N_2 in the headspace and <3 mM of HCO_3^- in the fluid produced only 10–20% of the organic acid concentrations in the N_2:CO_2 headspace experiments while generating similar concentrations of H_2. It appears Fe-oxidation reactions were occurring in both experiments, but much less carbon was available in the N_2-only controls.

The production of low molecular weight organic molecules does not account for all of the carbon lost from the headspace; there is a missing sink of carbon. An average of 1.9 μmol (SW) and 4.6 μmol (RW) organic acids were generated whereas ~250 μmol of headspace CO_2 is consumed in RW media and ~170 μmol of headspace CO_2 is consumed in SW media (Supplementary Table 5).

We do not observe abiotic formation of CH_4 at 100 °C. CH_4 has been observed as a product in water/rock reaction experiments at 30, 50 and 70 °C in previous studies, but it is unclear if such CH_4 formed as the result of the water/rock reactions or was released from fluid inclusions or the butyl stoppers used in the experiment (Neubeck et al., 2011; Okland et al., 2014). Nor do we observe carbonate formation (Supplementary Table 2). This may be due to kinetic limitations in precipitating dolomite and magnesite at low temperatures (Giammar et al., 2005; Hänchen et al., 2008), the high water/rock ratios in our experiments, or the pervasive reduction of carbon during ongoing H_2 production. Another possible sink of carbon in these experiments is abiotic solid carbonaceous material (Milesi et al., 2016). It is challenging to spectroscopically identify because it can be concentrated in rare blebs or coating mineral surfaces as a small fraction of a wt% compared to the mineral components. Using our mass-balance calculations, there could be ~14 mmol of particulate carbon forming in SW experiments and ~20 mmol of carbon forming in RW experiments. Such a small amount of carbon is difficult to measure by standard total organic carbon combustion techniques, which analyze <100 mg of sample at a time. Therefore, although our TOC analysis does not show the presence of solid carbon, it is below the detection limit.

5. CONCLUSIONS

The hydration of Oman dunite in anoxic, CO_2-bearing fluids produces as much or more H_2 as similar, previous low-temperature laboratory experiments (Neubeck et al., 2011; Okland et al., 2012, 2014; Mayhew et al., 2013). A key control on the amount of hydrogen generated is the solubility of Fe(II)-bearing phases such as brucite, which can be sensitively modulated by the fluid chemistry. The reacted mineral assemblage in our experiments still contains abundant Fe(II), thus it stores significant reducing potential and long-term reactivity. We predict that Oman dunite is capable of producing one to two orders more H_2 than we observed based on remaining Fe(II). However, the conditions under which the additional Fe can be released and oxidized are enigmatic. Additionally, although significant CO_2 consumption occurs, no carbonate minerals form and not all of the lost C is sequestered into observed quantities of organic acids. Amorphous solid carbon species may have also formed; however, such carbon has not been directly verified.

It remains challenging to conduct low-temperature anoxic water/rock reactions due to the slow reaction rates and small amounts of reaction products. Silica serum vials capped with butyl rubber stoppers are not ideal for continuously measuring low levels of hydrogen production. They contribute background concentrations of hydrogen and organic compounds, as well as dissolved silica, which can alter the reaction products. Follow-up work should focus on conducting similar peridotite hydration experiments in gas-tight, non-reactive vessels that allows periodic sampling of the aqueous and mineral components. These experiments should also use HCO_3^- with a ^{13}C label to track the fate of dissolved C and unequivocally demonstrate the presence, or absence, of organic synthesis reactions. Moreover, the effects of pH, silica activity, ionic strength, and temperature need to be clearly constrained and experimentally tested at low temperatures to better pinpoint the operative hydrogen-producing reactions in subsurface serpentinizing systems.

Overall, partially-serpentinized rocks have the potential to generate significant amounts of hydrogen due to oxidation of Fe(II)-bearing brucite, as well as produce organic acids at low temperatures. The H_2 and organic acids produced during the alteration of partially-serpentinized dunite could support subsurface rock-hosted life. Low levels of dissolved HCO_3^- and oxidants can fuel metabolisms such as methanogenesis, acetogenesis, sulfate reduction and metal-reduction pathways.

ACKNOWLEDGEMENTS

The authors would like to thank numerous colleagues at the University of Colorado at Boulder: Julien Allaz and the electron microprobe lab, Fred Luiszer at the Laboratory for Environmental and Geological Studies. We also thank Masako Tominaga (TAMU), who conducted the magnetic susceptibility analyses, and Mark Conrad (LBNL) who contributed the carbonate quantification and $\delta^{13}C$ measurements. Raman imaging and spectroscopy was conducted at the Raman Microspectroscopy Laboratory at the Department of Geological Sciences, University of Colorado-Boulder. This research was funded primarily by the Department of Energy (DE-SC0006886), with supporting work conducted through the Rock-Powered Life NASA Astrobiology Institute (Cooperative Agreement NNA15BB02A). Use of the Stanford Synchrotron Radiation Lightsource, SLAC National Accelerator Laboratory, is supported by the U.S. Department of Energy, Office of Science, Office of Basic Energy Sciences under Contract No. DE-AC02-76SF00515, in collaboration with staff scientists Sam Webb, Courtney Krest, and Ryan Davis. We also thank Franck Bourdelle (Université des Sciences et Technologies de Lille 1) and Manuel Munoz (Institut des Sciences de la Terre, Universite Joseph Fourier) for providing standards for our Fe(II/III) analysis.

APPENDIX A. SUPPLEMENTARY MATERIAL

Supplementary data associated with this article can be found, in the online version, at http://dx.doi.org/10.1016/j.gca.2017.04.022.

REFERENCES

Abrajano T. A., Sturchio N. C., Kennedy B. M., Lyon G. L., Muehlenbachs K. and Bohlke J. K. (1990) Geochemistry of reduced gas related to serpentinization of the Zambales ophiolite, Philippines. *Appl. Geochem.* **5**, 625–630.

Anderson R. T., Chapelle F. H. and Lovley D. R. (1998) Evidence against hydrogen-based microbial ecosystems in basalt aquifers. *Science* **281**, 976–977.

Andreani M., Muñoz M., Marcaillou C. and Delacour A. (2013) MXANES study of iron redox state in serpentine during oceanic serpentinization. *Lithos* **178**, 70–83.

Bach W. (2016) Some compositional and kinetic controls on the bioenergetic landscapes in oceanic basement. *Extreme Microbiol.* **107**.

Barnes I., O'Neil J. R. and Trescases J. J. (1978) Present day serpentinization in New Caledonia, Oman and Yugoslavia. *Geochim. Cosmochim. Acta* **42**, 144–145.

Béarat H., McKelvy M. J., Chizmeshya A. V. G., Gormley D., Nunez R., Carpenter R. W., Squires K. and Wolf G. H. (2006) Carbon sequestration via aqueous olivine mineral carbonation: role of passivating layer formation. *Environ. Sci. Technol.* **40**, 4802–4808.

Boudier F., Baronnet A. and Mainprice D. (2010) Serpentine mineral replacements of natural olivine and their seismic implications: oceanic lizardite versus subduction-related antigorite. *J. Petrol.* **51**, 495–512.

Coey J. M. D., Ballet O., Moukarika A. and Soubeyroux J. L. (1981) Magnetic properties of sheet silicates; 1:1 layer minerals. *Phys. Chem. Miner.* **7**, 141–148.

Coleman R. G. (1981) Tectonic setting for ophiolite obduction in Oman. *J. Geophys. Res. Solid Earth* **86**, 2497–2508.

Crespo-Medina M., Twing K. I., Kubo M. D. Y., Hoehler T. M., Cardace D., McCollom T. and Schrenk M. O. (2014) Insights into environmental controls on microbial communities in a continental serpentinite aquifer using a microcosm-based approach. *Front. Microbiol.* **5**. Available at: <http://www.ncbi.nlm.nih.gov/pmc/articles/PMC4231944/ (accessed September 1, 2015).

Debret B., Andreani M., Muñoz M., Bolfan-Casanova N., Carlut J., Nicollet C., Schwartz S. and Trcera N. (2014) Evolution of Fe redox state in serpentine during subduction. *Earth Planet. Sci. Lett.* **400**, 206–218.

Eberl D. D. (2003) *User Guide to RockJock - A Program for Determining Quantitative Mineralogy from X-Ray Diffraction Data*. U.S. Geological Survey. Available at: <http://pubs.er.usgs.gov/publication/ofr200378> (accessed January 29, 2016).

Ehlmann B. L., Mustard J. F. and Murchie S. L. (2010) Geologic setting of serpentine deposits on Mars: SERPENTINE ON MARS. *Geophys. Res. Lett.* **37**, n/a-n/a.

Elmaleh A., Tarantino S. C., Zema M., Devouard B. and Fialin M. (2012) The low-temperature magnetic signature of Fe-rich serpentine in CM2 chondrites: comparison with terrestrial cronstedtite and evolution with the degree of alteration. *Geochem. Geophys. Geosystems.* **13**, Q05Z42.

Espinosa A., Serrano A., Llavona A., Morena de la J. J., Abuin M., Figuerola A., Pellegrino T., Fernández J. F., Garcia-Hernandez M., Castro G. R. and Garcia M. A. (2012) On the discrimination between magnetite and maghemite by XANES measurements in fluorescence mode. *Meas. Sci. Technol.* **23**, 15602.

Etiope G., Schoell M. and Hosgörmez H. (2011) Abiotic methane flux from the Chimaera seep and Tekirova ophiolites (Turkey): understanding gas exhalation from low temperature serpentinization and implications for Mars. *Earth Planet. Sci. Lett.* **310**, 96–104.

Evans B. W., Kuehner S. M. and Chopelas A. (2009) Magnetite-free, yellow lizardite serpentinization of olivine websterite, Canyon Mountain complex, N.E. Oregon. *Am. Mineral.* **94**, 1731–1734.

Frost B. R. and Beard J. S. (2007) On silica activity and serpentinization. *J. Petrol.* **48**, 1351–1368.

Frost B. R., Evans K. A., Swapp S. M., Beard J. S. and Mothersole F. E. (2013) The process of serpentinization in dunite from New Caledonia. *Lithos* **178**, 24–39.

Fyfe W. S. (1974) Heats of chemical reactions and submarine heat production. *Geophys. J. R. Astron. Soc.* **37**, 213–215.

Giammar D. E., Bruant, Jr., R. G. and Peters C. A. (2005) Forsterite dissolution and magnesite precipitation at conditions relevant for deep saline aquifer storage and sequestration of carbon dioxide. *Chem. Geol.* **217**, 257–276.

Glein C. R., Baross J. A. and Waite, Jr., J. H. (2015) The pH of Enceladus' ocean. *Geochim. Cosmochim. Acta* **162**, 202–219.

Groppo C., Rinaudo C., Cairo S., Gastaldi D. and Compagnoni R. (2006) Micro-Raman spectroscopy for a quick and reliable identification of serpentine minerals from ultramafics. *Eur. J. Mineral.* **18**, 319–329.

Hänchen M., Prigiobbe V., Storti G., Seward T. M. and Mazzotti M. (2006) Dissolution kinetics of fosteritic olivine at 90–150 °C including effects of the presence of CO_2. *Geochim. Cosmochim. Acta* **70**, 4403–4416.

Hänchen M., Prigiobbe V., Baciocchi R. and Mazzotti M. (2008) Precipitation in the Mg-carbonate system—effects of temperature and CO_2 pressure. *Chem. Eng. Sci.* **63**, 1012–1028.

Hanghøj K., Kelemen P. B., Hassler D. and Godard M. (2010) Composition and genesis of depleted mantle peridotites from the Wadi Tayin Massif, Oman Ophiolite; major and trace element geochemistry, and Os isotope and PGE systematics. *J. Petrol.* **51**, 201–227.

Hoal K. O., Appleby S. K., Stammer J. G. and Palmer C. (2009) SEM-based quantitative mineralogical analysis of peridotite, kimberlite, and concentrate. *Lithos* **112**(Suppl. 1), 41–46.

Jetten M. S., Stams A. J. and Zehnder A. J. (1992) Methanogenesis from acetate: a comparison of the acetate metabolism in *Methanothrix soehngenii* and *Methanosarcina* spp.. *FEMS Microbiol. Rev.* **88**, 181–197.

Jöns N., Bach W. and Klein F. (2010) Magmatic influence on reaction paths and element transport during serpentinization. *Chem. Geol.* **274**, 196–211.

Kelemen P. B. and Matter J. (2008) In situ carbonation of peridotite for CO_2 storage. *Proc. Natl. Acad. Sci.* **105**, 17295–17300.

Kelemen P. B., Hirth G., Shimizu N., Spiegelman M. and Dick H. J. (1997) A review of melt migration processes in the adiabatically upwelling mantle beneath oceanic spreading ridges. *Philos. Trans. R. Soc. Lond. Math. Phys. Eng. Sci.* **355**, 283–318.

Kelemen P. B., Matter J., Streit E. E., Rudge J. F., Curry W. B. and Blusztajn J. (2011) Rates and mechanisms of mineral carbonation in peridotite: natural processes and recipes for enhanced, in situ CO_2 capture and storage. *Annu. Rev. Earth Planet. Sci.* **39**, 545–576.

Kim W., Suh C.-Y., Cho S.-W., Roh K.-M., Kwon H., Song K. and Shon I.-J. (2012) A new method for the identification and quantification of magnetite–maghemite mixture using conventional X-ray diffraction technique. *Talanta* **94**, 348–352.

Klein F., Bach W., Jöns N., McCollom T., Moskowitz B. and Berquó T. (2009) Iron partitioning and hydrogen generation during serpentinization of abyssal peridotites from 15°N on the Mid-Atlantic Ridge. *Geochim. Cosmochim. Acta* **73**, 6868–6893.

Klein F., Bach W. and McCollom T. M. (2013) Compositional controls on hydrogen generation during serpentinization of ultramafic rocks. *Lithos* **178**, 55–69.

Klein F., Grozeva N. G., Seewald J. S., McCollom T. M., Humphris S. E., Moskowitz B., Berquó T. S. and Kahl W.-A. (2015) Experimental constraints on fluid-rock reactions during incipient serpentinization of harzburgite. *Am. Miner.* **100**, 991–1002.

Kral T. A., Brink K. M., Miller S. L. and McKay C. P. (1998) Hydrogen consumption by methanogens on the early Earth. *Orig. Life Evol. Biosph.* **28**, 311–319.

Lang S. Q., Butterfield D. A., Schulte M., Kelley D. S. and Lilley M. D. (2010) Elevated concentrations of formate, acetate and dissolved organic carbon found at the Lost City hydrothermal field. *Geochim. Cosmochim. Acta* **74**, 941–952.

Malvoisin B., Brunet F., Carlut J., Rouméjon S. and Cannat M. (2012) Serpentinization of oceanic peridotites: 2. Kinetics and processes of San Carlos olivine hydrothermal alteration. *J. Geophys. Res. Solid Earth* **117**, n/a-n/a.

Malvoisin B., Carlut J. and Brunet F. (2012) Serpentinization of oceanic peridotites: 1. A high-sensitivity method to monitor magnetite production in hydrothermal experiments. *J. Geophys. Res. Solid Earth* **117**, B01104.

Mayhew L. E., Ellison E. T., McCollom T. M., Trainor T. P. and Templeton A. S. (2013) Hydrogen generation from low-temperature water–rock reactions. *Nat. Geosci.* **6**, 478–484.

McCollom T. M. and Bach W. (2009) Thermodynamic constraints on hydrogen generation during serpentinization of ultramafic rocks. *Geochim. Cosmochim. Acta* **73**, 856–875.

McCollom T. M. and Donaldson C. (2016) Generation of hydrogen and methane during experimental low-temperature reaction of ultramafic rocks with water. *Astrobiology*. Available at: <http://online.liebertpub.com/doi/abs/10.1089/ast.2015.1382> (accessed June 6, 2016).

McCollom T. M. and Seewald J. S. (2001) A reassessment of the potential for reduction of dissolved CO_2 to hydrocarbons during serpentinization of olivine. *Geochim. Cosmochim. Acta* **65**, 3769–3778.

McCollom T. M. and Seewald J. S. (2003) Experimental constraints on the hydrothermal reactivity of organic acids and acid anions: I. Formic acid and formate. *Geochim. Cosmochim. Acta* **67**, 3625–3644.

McCollom T. M., Klein F., Robbins M., Moskowitz B., Berquó T. S., Jöns N., Bach W. and Templeton A. (2016) Temperature trends for reaction rates, hydrogen generation, and partitioning of iron during experimental serpentinization of olivine. *Geochim. Cosmochim. Acta* **181**, 175–200.

McDermott J. M., Seewald J. S., German C. R. and Sylva S. P. (2015) Pathways for abiotic organic synthesis at submarine hydrothermal fields. *Proc. Natl. Acad. Sci.*, 201506295.

Milesi V., McCollom T. M. and Guyot F. (2016) Thermodynamic constraints on the formation of condensed carbon from serpentinization fluids. *Geochim. Cosmochim. Acta* **189**, 391–403.

Miller H. M., Matter J. M., Kelemen P., Ellison E. T., Conrad M. E., Fierer N., Ruchala T., Tominaga M. and Templeton A. S. (2016) Modern water/rock reactions in Oman hyperalkaline peridotite aquifers and implications for microbial habitability. *Geochim. Cosmochim. Acta* **179**, 217–241.

Morrill P. L., Kuenen J. G., Johnson O. J., Suzuki S., Rietze A., Sessions A. L., Fogel M. L. and Nealson K. H. (2013) Geochemistry and geobiology of a present-day serpentinization site in California: The Cedars. *Geochim. Cosmochim. Acta* **109**, 222–240.

Morrill P. L., Brazelton W. J., Kohl L., Rietze A., Miles S. M., Kavanagh H., Schrenk M. O., Ziegler S. E. and Lang S. Q.

(2014) Investigations of potential microbial methanogenic and carbon monoxide utilization pathways in ultra-basic reducing springs associated with present-day continental serpentinization: the Tablelands, NL, CAN. *Front. Microbiol.* **5**. Available at: <http://www.ncbi.nlm.nih.gov/pmc/articles/PMC4230201/> (accessed January 6, 2015).

Muñoz M., Vidal O., Marcaillou C., Pascarelli S., Mathon O. and Farges F. (2013) Iron oxidation state in phyllosilicate single crystals using Fe-K pre-edge and XANES spectroscopy: effects of the linear polarization of the synchrotron X-ray beam. *Am. Miner.* **98**, 1187–1197.

Neal C. and Stanger G. (1983) Hydrogen generation from mantle source rocks in Oman. *Earth Planet. Sci. Lett.* **66**, 315–320.

Neal C. and Stanger G. (1984) Calcium and magnesium hydroxide precipitation from alkaline groundwaters in Oman, and their significance to the process of serpentinization. *Miner. Mag.* **48**, 237–241.

Nealson K. H., Inagaki F. and Takai K. (2005) Hydrogen-driven subsurface lithoautotrophic microbial ecosystems (SLiMEs): do they exist and why should we care? *Trends Microbiol.* **13**, 405–410.

Neubeck A., Duc N. T., Bastviken D., Crill P. and Holm N. G. (2011) Formation of H_2 and CH_4 by weathering of olivine at temperatures between 30 and 70 °C. *Geochem. Trans.* **12**, 6.

Neubeck A., Duc N. T., Hellevang H., Oze C., Bastviken D., Bacsik Z. and Holm N. G. (2014) Olivine alteration and H_2 production in carbonate-rich, low temperature aqueous environments. *Planet. Space Sci.* **96**, 51–61.

Neubeck A., Nguyen D. T. and Etiope G. (2015) Low-temperature dunite hydration: evaluating CH4 and H2 production from H_2O and CO_2. *Geofluids*, n/a-n/a.

Ogasawara Y., Okamoto A., Hirano N. and Tsuchiya N. (2013) Coupled reactions and silica diffusion during serpentinization. *Geochim. Cosmochim. Acta* **119**, 212–230.

Okland I., Huang S., Dahle H., Thorseth I. H. and Pedersen R. B. (2012) Low temperature alteration of serpentinized ultramafic rock and implications for microbial life. *Chem. Geol.* **318–319**, 75–87.

Okland I., Huang S., Thorseth I. H. and Pedersen R. B. (2014) Formation of H_2, CH_4 and N-species during low-temperature experimental alteration of ultramafic rocks. *Chem. Geol.* **387**, 22–34.

Oremland R. S., Miller L. G. and Whiticar M. J. (1987) Sources and flux of natural gases from Mono Lake, California. *Geochim. Cosmochim. Acta* **51**, 2915–2929.

Oufi O., Cannat M. and Horen H. (2002) Magnetic properties of variably serpentinized abyssal peridotites. *J. Geophys. Res. Solid Earth* **107**, EPM 3-1.

Özdemir Ö. and Dunlop D. J. (2010) Hallmarks of maghemitization in low-temperature remanence cycling of partially oxidized magnetite nanoparticles. *J. Geophys. Res. Solid Earth* **115**, B02101.

Paukert A. N., Matter J. M., Kelemen P. B., Shock E. L. and Havig J. R. (2012) Reaction path modeling of enhanced in situ CO_2 mineralization for carbon sequestration in the peridotite of the Samail Ophiolite, Sultanate of Oman. *Chem. Geol.* **330–331**, 86–100.

Petriglieri J. R., Salvioli-Mariani E., Mantovani L., Tribaudino M., Lottici P. P., Laporte-Magoni C. and Bersani D. (2015) Micro-Raman mapping of the polymorphs of serpentine. *J. Raman Spectrosc.*, n/a-n/a.

Pokrovsky O. S. and Schott J. (2004) Experimental study of brucite dissolution and precipitation in aqueous solutions: surface speciation and chemical affinity control. *Geochim. Cosmochim. Acta* **68**, 31–45.

Pokrovsky O. S., Schott J. and Castillo A. (2005) Kinetics of brucite dissolution at 25 °C in the presence of organic and inorganic ligands and divalent metals. *Geochim. Cosmochim. Acta* **69**, 905–918.

Prigiobbe V., Costa G., Baciocchi R., Hänchen M. and Mazzotti M. (2009) The effect of and salinity on olivine dissolution kinetics at. *Chem. Eng. Sci.* **64**, 3510–3515.

Reynard B., Bezacier L. and Caracas R. (2015) Serpentines, talc, chlorites, and their high-pressure phase transitions: a Raman spectroscopic study. *Phys. Chem. Miner.* **42**, 641–649.

Rinaudo C., Gastaldi D. and Belluso E. (2003) Characterization of chrysotile, antigorite and lizardite by ft-raman spectroscopy. *Can. Mineral.* **41**, 883–890.

Russell M. J. and Martin W. (2004) The rocky roots of the acetyl-CoA pathway. *Trends Biochem. Sci.* **29**, 358–363.

Russell M. J., Hall A. J. and Martin W. (2010) Serpentinization as a source of energy at the origin of life: serpentinization and the emergence of life. *Geobiology* **8**, 355–371.

Russell M. J., Nitschke W. and Branscomb E. (2013) The inevitable journey to being. *Philos. Trans. R. Soc. B* **368**, 20120254.

Schrenk M. O., Brazelton W. J. and Lang S. Q. (2013) Serpentinization, carbon, and deep life. *Rev. Mineral. Geochem.* **75**, 575–606.

Seewald J. S., Zolotov M. Y. and McCollom T. (2006) Experimental investigation of single carbon compounds under hydrothermal conditions. *Geochim. Cosmochim. Acta* **70**, 446–460.

Sekine Y., Shibuya T., Postberg F., Hsu H.-W., Suzuki K., Masaki Y., Kuwatani T., Mori M., Hong P. K., Yoshizaki M., Tachibana S. and Sirono S. (2015) High-temperature water–rock interactions and hydrothermal environments in the chondrite-like core of Enceladus. *Nat. Commun.* **6**, 8604.

Shibuya T., Yoshizaki M., Sato M., Shimizu K., Nakamura K., Omori S., Suzuki K., Takai K., Tsunakawa H. and Maruyama S. (2015) Hydrogen-rich hydrothermal environments in the Hadean ocean inferred from serpentinization of komatiites at 300 °C and 500 bar. *Prog. Earth Planet. Sci.* **2**, 46.

Shibuya T., Russell M. J. and Takai K. (2016) Free energy distribution and hydrothermal mineral precipitation in Hadean submarine alkaline vent systems: importance of iron redox reactions under anoxic conditions. *Geochim. Cosmochim. Acta* **175**, 1–19.

Shock E. L. and Schulte M. D. (1998) Organic synthesis during fluid mixing in hydrothermal systems. *J. Geophys. Res. Planets* **103**, 28513–28527.

Sleep N. H., Meibom A., Fridriksson T., Coleman R. G. and Bird D. K. (2004) H_2-rich fluids from serpentinization: geochemical and biotic implications. *Proc. Natl. Acad. Sci. USA* **101**, 12818–12823.

Spear J. R., Walker J. J., McCollom T. M. and Pace N. R. (2005) Hydrogen and bioenergetics in the Yellowstone geothermal ecosystem. *Proc. Natl. Acad. Sci. USA* **102**, 2555–2560.

Stevens T. O. and McKinley J. P. (1995) Lithoautotrophic microbial ecosystems in deep basalt aquifers. *Science* **270**, 450–455.

Stevens T. O. and McKinley J. P. (2000) Abiotic controls on H_2 production from basalt–water reactions and implications for aquifer biogeochemistry. *Environ. Sci. Technol.* **34**, 826–831.

Streit E., Kelemen P. and Eiler J. (2012) Coexisting serpentine and quartz from carbonate-bearing serpentinized peridotite in the Samail Ophiolite, Oman. *Contrib. Mineral. Petrol.* **164**, 821–837.

Suda K., Ueno Y., Yoshizaki M., Nakamura H., Kurokawa K., Nishiyama E., Yoshino K., Hongoh Y., Kawachi K., Omori S., Yamada K., Yoshida N. and Maruyama S. (2014) Origin of methane in serpentinite-hosted hydrothermal systems: the

CH_4–H_2–H_2O hydrogen isotope systematics of the Hakuba Happo hot spring. *Earth Planet. Sci. Lett.* **386**, 112–125.

Szponar N., Brazelton W. J., Schrenk M. O., Bower D. M., Steele A. and Morrill P. L. (2013) Geochemistry of a continental site of serpentinization, the Tablelands Ophiolite, Gros Morne National Park: a Mars analogue. *Icarus* **224**, 286–296.

Takai K., Nakamura K., Toki T., Tsunogai U., Miyazaki M., Miyazaki J., Hirayama H., Nakagawa S., Nunoura T. and Horikoshi K. (2008) Cell proliferation at 122 °C and isotopically heavy CH_4 production by a hyperthermophilic methanogen under high-pressure cultivation. *Proc. Natl. Acad. Sci.* **105**, 10949–10954.

Telling J., Boyd E. S., Bone N., Jones E. L., Tranter M., MacFarlane J. W., Martin P. G., Wadham J. L., Lamarche-Gagnon, Skidmore M. L., Hamilton T. L., Hill E., Jackson M. and Hodgson D. A. (2015) Rock comminution as a source of hydrogen for subglacial ecosystems. *Nat. Geosci.* **8**, 851–855.

Wilke M., Farges F., Petit P.-E., Brown G. E. and Martin F. (2001) Oxidation state and coordination of Fe in minerals: An Fe K-XANES spectroscopic study. *Am. Miner.* **86**, 714–730.

Zinder S. H. (1993) Physiological ecology of methanogens. In *Methanogenesis* (ed. D. J. G. Ferry). Chapman & Hall Microbiology Series, Springer, USA, pp. 128–206. Available at: <http://link.springer.com/chapter/10.1007/978-1-4615-2391-8_4> (accessed November 11, 2015).

Associate editor: Jun-ichiro Ishibashi